actuators

MDPI

Article

Static and Dynamic Characterization and Control of a High-Performance Electro-Hydraulic Actuator

Govind N. Sahu, Suyash Singh, Aditya Singh and Mohit Law *

Machine Tool Dynamics Laboratory, Department of Mechanical Engineering, Indian Institute of Technology Kanpur, Kanpur 208016, India; govinds@iitk.ac.in (G.N.S.); suyashsi@iitk.ac.in (S.S.); adisingh@iitk.ac.in (A.S.)
* Correspondence: mlaw@iitk.ac.in (M.L.); Tel.: +91-512-679-6897

Received: 28 May 2020; Accepted: 23 June 2020; Published: 25 June 2020

Abstract: This paper characterizes the static, dynamic, and controlled behavior of a high-performance electro-hydraulic actuator to assess its suitability for use in evaluating machine tool behavior. The actuator consists of a double-acting piston and cylinder arrangement controlled by a servo valve and a separate rear chamber controlled by a separate valve, designed to work in conjunction to generate static forces of up to 7000 N that can be superposed with dynamic forces of up to ± 1500 N. This superposition of periodic forces with a non-zero mean makes the actuator capable of applying realistic loading conditions like those experienced by machines during cutting processes. To characterize the performance of this actuator, linearized static and dynamic models are described. Since experiments with the actuator exhibit nonlinear characteristics, the linearized static model is expanded to include the influence of nonlinearities due to flow, leakages, saturations, and due to friction and hysteresis. Since all major nonlinearities are accounted for in the expanded static model, the dynamical model remains linear. Unknown static and dynamical model parameters are calibrated from experiments, and the updated models are observed to capture experimentally observed behavior very well. Validated models are used to tune the proportional and integral gains for the closed-loop control strategy, and the model-based tuning in turn guides appropriate closed-loop control of the actuator to increase its bandwidth to 200 Hz. The statically and dynamically characterized actuator can aid machine tool structural testing. Moreover, the validated models can instruct the design and development of other higher-performance electro-hydraulic actuators, guide the conversion of the actuator into a damper, and also test other advanced control strategies to further improve actuator performance.

Keywords: electro-hydraulic actuator; servo valve; static; dynamic; force; nonlinear; force feedback; control; machine tool

1. Introduction

Structural testing of machine tools to evaluate their static and dynamic characteristics involves loading the machine with scenarios experienced under real cutting conditions. Since real loading conditions often involve a periodic force that modulates about a non-zero mean, and since commonly used modal hammers and/or electrodynamic shakers cannot provide such excitations, this paper reports on the characteristics of a newly developed high-performance electro-hydraulic actuator to evaluate its suitability for its use in machine tool structural testing applications.

Electro-hydraulic actuators, because of their high stiffness-to-weight ratios, their high force capabilities, their large strokes, and their relatively quick response, have found applications across many engineering domains. Applications include their use in manufacturing and industrial machinery [1–3], farm and earth moving equipment [4], machine tools [5–15], testing equipment [16,17], flight simulation and control [18,19], automotive and robotics [20], and in numerous other domains. Since actuators are designed and characterized as per their applications, and since this

paper is concerned with electro-hydraulic actuators for their use in the static and dynamic testing of machine tool structural systems, discussions herein are circumscribed by the application of interest.

Even though electro-hydraulic actuators have found use in machine tools, their use has mainly been limited to provide motion to the table and/or the tool [5–8], to effectively damp machine tool vibrations [9–11], and to isolate machines from ground vibrations [12–14]. Though machine tool structural testing using electro-hydraulic actuators is routine across many research labs, oddly, besides the study reporting the design and development of actuators for vibration testing [15], there appear no other reports discussing the characteristics of electro-hydraulic actuators for machine tools.

Furthermore, despite the wide use of electro-hydraulic actuators across domains, and despite of the advantages they offer over other kinds of actuators, the static and dynamic characteristics of these electro-hydraulic systems are nonlinear, and understanding and characterizing these nonlinearities are essential to enable effective use and control of the actuators. Typical nonlinearities arise due to electrical hysteresis in the torque motor of the servo valve [1,2,21–23], due to dead-band related nonlinearities in the servo valve [1,2,21,24–26], due to pressure drops on account of leakages in actuator-servo valve assembly [1,2,23,24,27–31], due to friction present in the piston-cylinder arrangement [1,2,23,25–29,32–36], and due to variations in the operating fluid temperature [2,25,37].

Even though these nonlinearities exist, some reported work of the use of electro-hydraulic actuators across other engineering domains have assumed a linearized model of the system [1,2,12–15,23,38–41], while some other reports for actuators used across other engineering domains have characterized some of these nonlinearities [25–37]. However, there are no reports detailing the nonlinear behavior of electro-hydraulic actuators used in machine tools. Furthermore, even though there are some reports on the static and dynamic characteristics of electro-hydraulic actuators used across other engineering domains [1,2,23,24,29,31,39,40], there are no such reports for actuator behavior for testing of machine tools. Moreover, since the actuator and the machine tool to be tested, both exhibit nonlinear behavior, it is paramount to decouple the nonlinear characteristics of the actuator from that of the machine. To do so, the nonlinear static and dynamic behavior of the electro-hydraulic actuator must be characterized separately and systematically.

Seeing that there is a need for an electro-hydraulic actuator that can apply periodic forces modulating about a non-zero mean for the static and dynamic testing of machine tool behavior under realistic loading scenarios, and that there exist no detailed reports characterizing the actuator behavior, this paper reports on the characteristics of the newly developed high-performance electro-hydraulic actuator to assess its suitability for its use in machine tool structural testing applications.

The constructional details of the newly developed composite and compact actuator are presented in Section 2 of the paper. The actuator consists of a double-acting piston and cylinder arrangement controlled by a servo valve, and a separate rear chamber controlled by a separate valve that are designed to work in conjunction to generate static forces up to 7000 N that can be superposed with dynamic forces of up to $\pm$ 1500 N with a targeted operational bandwidth of 200 Hz. The superposition of static and dynamic forces meets the machine tool requirement of generating periodic forces with a non-zero mean, and the bandwidth of 200 Hz will enable excitation of the low frequency global structural modes of machine tools [42]. Though the composite design of the actuator is like that reported in [15,39,40], the force capacity, the bandwidth, and the expanded model-based systematic analysis presented in Sections 3 and 4 in this paper is unlike any in the literature.

Experiments in Section 4 of the paper for different voltages and pressures show the static behavior of the electro-hydraulic actuator to be nonlinear. Characterization of the nonlinear static behavior of the actuator is separately presented for flow control by the servo valve to the main piston chambers, and separately for the pressure reducing valve controlling flow to the rear chamber. Static models for both cases are expanded to include the nonlinear flow characteristics of the servo valve and actuator assembly. These include accounting for the presence of dead-bands, for friction and frictional hysteresis, for leakages, for saturation behavior, and for even the effects of fluid temperature on the force response. Unknown model parameters in each case are identified from experiments, and the expanded nonlinear static model is observed to capture experimentally observed behavior very well, as is also discussed in Section 4. Such expanded and comprehensive

modelling of all the key nonlinearities observed in typical electro-hydraulic actuators, as is done in this paper, we believe, is unlike any other investigation reported in the literature. Furthermore, characterization of the actuator's behavior under pressurized flow to the rear chamber, as is presented in this paper, is new, and has not been reported on by others.

Dynamic experimental characteristics are discussed in Section 5 of the paper. Those experiments include a dynamic force component superposed with a static component. The dynamic model is also updated by identifying unknown model parameters from experiments. Following the reports in [39,40], herein too, we assume that since most nonlinearities are accounted for in the static model, and since nonlinearities are due to the static friction, due to variations in the flow-pressure coefficient of the servo valve, due to leakages causing pressure drops, and due to that valve overlaps do not strongly depend on the operating frequency, the updated dynamic model remains linear, and results with it are found to reasonably agree with experiments–as is also discussed in Section 5.

Models and experiments presented in Sections 3, 4, and 5 are all for the open-loop configuration of the electro-hydraulic actuator, with closed-loop control being separately addressed in Section 6 of the paper. Closed-loop control is based on force feedback, such as reported in [28,43–47]. Since the objective of closed-loop control is to target a bandwidth of 200 Hz, a simple proportional-integral (PI) controller is preferred herein. The validated static and dynamic models are used to tune gains for the closed-loop control strategy, and the model-based tuning in turn guides appropriate closed-loop control of the actuator. On having systematically characterized the nonlinear static and dynamic behavior of the actuator and its control, the paper is finally concluded.

2. Constructional Details and Working Principle of the Electro-Hydraulic Actuator

A schematic and the experimental setup of the electro-hydraulic actuator mounted on a rigid bracket is shown in Figure 1a,b, respectively. The composite design of a double-acting piston and cylinder arrangement controlled by a servo valve, and a separate rear chamber controlled by a pressure reducing valve is evident from the schematic in Figure 1a. The piston applies force against a rigid block. The block and the bracket (on which the actuator is mounted) are rigidly secured to a rigid bed to minimize the influence of boundary conditions.

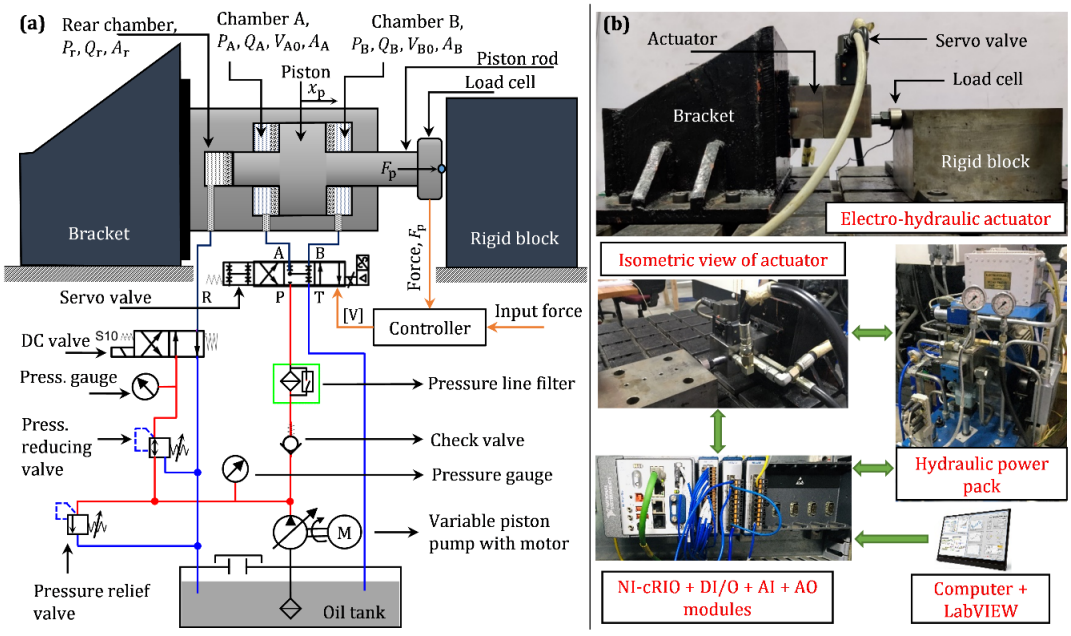

Figure 1. (**a**) Schematic of the electro-hydraulic actuator; (**b**) the experimental setup.

The electro-hydraulic actuator can be thought to be divided into five (sub)systems as: (1) the power supply, (2) the hydraulic unit, (3) the hydro-mechanical, (4) the control hardware, and (5) the

control software. An overview of the flow of information form/to the various (sub)systems of the electro-hydraulic actuator is shown in Figure 2.

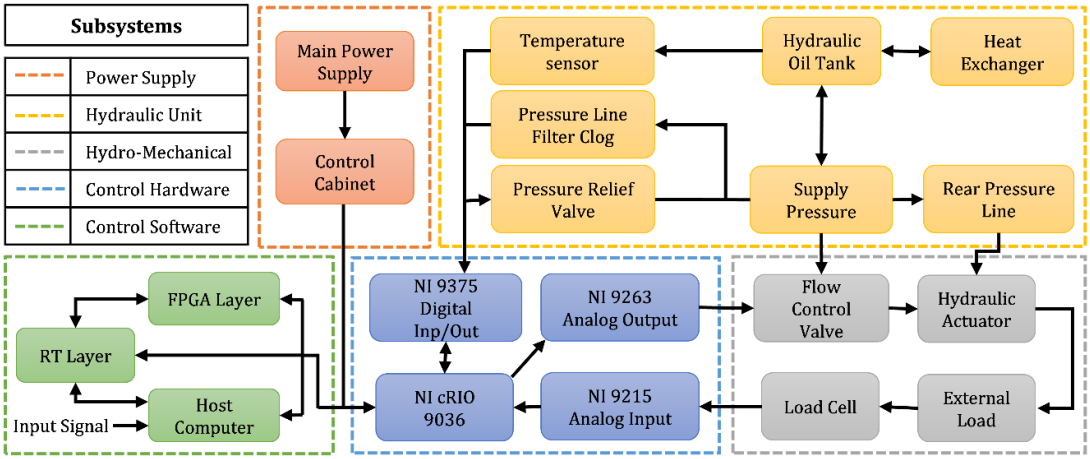

Figure 2. Schematic overview showing the flow of information to/from various (sub)systems of the electro-hydraulic actuator.

Main elements and functions of each of the (sub)systems shown in Figure 2 is described as follows:

1. Power supply: the power supply unit consist of an electrical unit connected to the main electrical supply line (3 phase, 400 V, 12 A, 50 Hz) that drives the hydraulic motor (Make: Rotomotive, specifications: 5.6 kW, 415 V, 1440 rpm, 50 Hz). The power unit also consists of a control transformer (output–230 V, 1kVA, 1 phase) and a control cabinet with a universal power supply (UPS) within it to power the servo valve in case of loss of power supply from the main line. The control cabinet houses several circuit breakers and a control chassis that in turn houses a controller, an analog-to-digital converter, and a digital-to-analog converter. The controller communicates with control hardware and software as detailed under.
2. Hydraulic unit: the hydraulic unit consists of a hydraulic tank, a hydraulic motor, a heat exchanger, and flow, pressure, and direction-controlled valves as well as essential auxiliary elements such as pressure gauges. The hydraulic power pack also has a sensor to monitor oil temperature and another to monitor blockages in the pressure lines. The power pack is connected to the actuator-servo valve assembly through three pipelines, which include the main supply pressure line (denoted as P), the rear supply line (denoted as R) and the return line to oil tank (denoted as T), see Figure 1a. The supply pressure line bears a maximum pressure of 21 MPa which is generated by the variable piston pump (Make: Nachi, Model number: HPP-NACHI + PVS-1B-16N3-12), controlled through a nozzle flapper type 4-way directional control servo valve (Make: Rexroth, Model number: 4WSE2EM6-2/2089ET210K17EV). Though the rear supply line is also fed by the main supply pressure line, its pressure can be regulated independently through the pressure reducing valve (Make: Nachi, Model number: 0G-G01-P2-21) and the flow direction can be controlled by a direction control valve (Make: Nachi, Model number: SA-G01-A3X-K-D2-31(D SPOOL)). The rear supply line is connected to the rear chamber, and pressurized fluid supplied to the rear chamber can be used to apply static forces over and above the static forces generated by the main piston chamber A and B, wherein flow control is achieved using the servo valve. The return line is a low-pressure line used to drain out the hydraulic oil from actuator assembly to the oil tank. The hydraulic unit also consists of a pressure relief valve (Make: Nachi, Model number: OR-G01-P3-20).
3. Hydro-mechanical: the major component of this unit is the actuator-piston-servo valve assembly. The actuator has been designed with a static force capacity of 7000 N over which dynamic forces up to $\pm$ 1500 N can be applied. A load cell (Make: IPA, Model number: LP013L1)

is installed on to the piston rod to measure the force applied by the actuator against the rigid structure. The load cell is a compressive-type device and hence the experiments are designed such that during operation the load cell must always be in contact with the structure under test. The actuator has a stroke of ± 5 mm, a piston diameter of 25 mm, a piston rod diameter of 18 mm, a total weight of about 6 kg, a maximum flow capacity of 15 lpm and a maximum working pressure of 21 MPa. The piston annulus is provided with rubber seals to reduce any leakages across the piston chambers.

4. Control hardware: the control hardware consists of a NI cRIO-9036 controller with a chassis that supports an analog input device (NI 9215) that measures the load, an analog output device (NI 9263) that commands the flow to the valve, and a digital input/output device (NI 9375) that is used to monitor different sensors on the hydraulic unit. Flow of information to/from these devices is shown schematically in Figure 2. These devices are controlled and monitored using a control software.
5. Control software: NI LabVIEW is used as the control software to monitor and to control the electro-hydraulic actuator. The LabVIEW program is divided into three subprograms to increase computational efficiency. These are: the FPGA (Field Programmable Gate array) layer which includes data acquisition and a proportional-integral (PI) controller–that is used in the closed-loop control of the actuator as detailed in Section 6; the RT (Real-Time) layer that displays time and frequency content of signals; and the Host layer that can generate any user-defined signal as necessary. The host layer also logs all signals of interest. The software layer also consists of a graphical user interface (GUI) as shown in Figure 3. This GUI is used to control and to monitor the electro-hydraulic actuator.

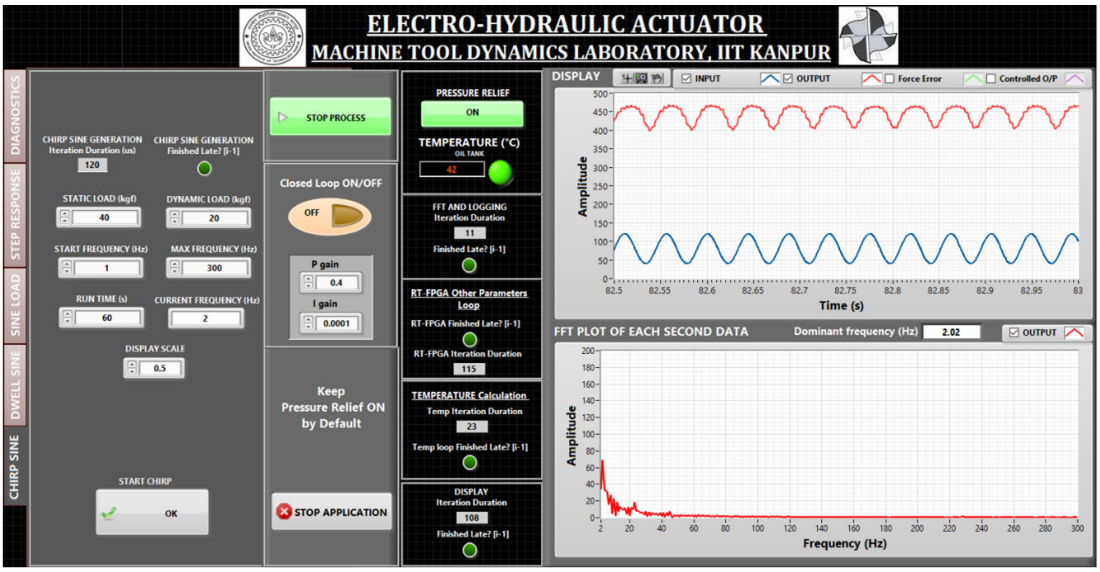

Figure 3. LabVIEW-based graphical user interface (GUI) for the operation of electro-hydraulic actuator.

Having detailed the constructional details of the actuator along with function of all its (sub) systems and its main elements, we now discuss the static and the dynamic model for this actuator to help describe its behavior.

3. Linearized Static and Dynamic Model of the Electro-Hydraulic Actuator

This section presents linearized models to characterize the static and dynamic force behavior of the actuator. These models are expanded subsequently as discussed in Section 4, to include nonlinearities. The models presented herein build on those reported in [1,2], and are like the linear models described elsewhere in [12–15,26,39–41]. Models described herein assume that the static and

dynamic behavior can be superposed over each other, and as such, at first, we only present the dynamic model, which is subsequently reduced to a static one.

3.1. Dynamic Force Model of the Actuator

The dynamic force response of the electro-hydraulic system is governed by the dynamics of the servo valve and of the hydro-mechanical system. These components are modelled separately, and the overall system is defined as the series combination of the valve and the hydro-mechanical system. The dynamical model assumes that no pressurized flow is supplied to the rear chamber.

3.1.1. Dynamics of the Servo Valve

The servo valve is a high gain electro-hydraulic transducer which converts command voltage signal to pressure difference across the piston chambers. Though servo valves have nonlinear characteristics and though their dynamics are influenced by variations in the orifice sizes, changes in the supply pressure, dead bands, internal leakages, and electrical hysteresis in torque motor, the valve is often linearized using a second-order transfer function for high bandwidth operation [1,2,13,38–41], and the general form of the transfer function of the linearized servo valve is given by:

$$G_{\text{valve}} = \frac{x_{\text{v}}}{v}(s) \equiv \frac{K_{\text{v}}}{(s/\omega_{\text{nv}})^2 + (2\zeta/\omega_{\text{nv}})s + 1}, \tag{1}$$

where x_{v} is the spool valve displacement (m) measured from the neutral position, v is the command voltage (V), K_{v} is a servo valve voltage gain (m/V), and ζ and ω_{nv} are the apparent damping ratio and natural frequency (rad/s) of the valve respectively.

3.1.2. Valve Flow and Chamber Pressure

The flow through the valve pressurizes the chamber plates of the actuator imparting a translatory motion to the piston, and for a critically centred spool, the flow is given by [2]:

$$Q = Q(x_{\text{v}}, \Delta P) \equiv c_{\text{v}} x_{\text{v}} \sqrt{|\Delta P|}\, sign(\Delta P), \tag{2}$$

where $c_{\text{v}} = \pi d_{\text{v}} c_{\text{d}} \sqrt{2/\rho}$ is the flow coefficient of the valve orifice, d_{v} is the diameter of the spool, c_{d} is the coefficient of the discharge, ρ is the density of the operating oil, and ΔP is the pressure difference across the valve orifice.

For a symmetric valve with a symmetric piston cylinder, and similar orifice diameters, the load pressure (P_{L}) becomes: $P_{\text{L}} = P_{\text{A}} - P_{\text{B}}$, and the load flow rate (Q_{L}) becomes: $Q_{\text{L}} = (Q_{\text{A}} + Q_{\text{B}})/2$.

Using the continuity equation, and assuming pressure in each chamber to be uniformly distributed, and neglecting leakages, flow through both chambers becomes equal, i.e., $Q_{\text{A}} = Q_{\text{B}}$, and the relationship between the supply pressure (P_{S}), the tank pressure (P_{T}) and the pressure in both chambers lead to: $P_{\text{S}} + P_{\text{T}} = P_{\text{A}} + P_{\text{B}}$. Using Equation (2) and aforementioned relationships, the load flow can be expressed as a function of valve position and load pressure as:

$$Q_{\text{L}} = \frac{c_{\text{v}} x_{\text{v}}}{\sqrt{2}} \sqrt{P_{\text{S}} - P_{\text{T}} - sign(x_{\text{v}}) P_{\text{L}}}\,. \tag{3}$$

Linearizing Equation (3) using the Taylor's expansion of $Q_{\text{L}}(x_{\text{v}}, P_{\text{L}})$ up to the first term about a particular operational point $P_0 = (x_{\text{v}_0}, P_{\text{A}_0}, P_{\text{B}_0})$, we get:

$$\Delta Q_{\text{L}} = \left.\frac{\partial Q_{\text{L}}}{\partial x_{\text{v}}}\right|_{P_0} \Delta x_{\text{v}} + \left.\frac{\partial Q_{\text{L}}}{\partial P_{\text{L}}}\right|_{P_0} \Delta P_{\text{L}}, \tag{4}$$

where we define $K_{\text{Q}} = \left.\frac{\partial Q_{\text{L}}}{\partial x_{\text{v}}}\right|_{P_0}$ as the valve flow coefficient (m^2/s), and $K_{\text{C}} = -\left.\frac{\partial Q_{\text{L}}}{\partial P_{\text{L}}}\right|_{P_0}$ as the valve flow-pressure coefficient ($\text{m}^3/\text{s/Pa}$) such that:

$$\Delta Q_{\text{L}} = K_{\text{Q}} \Delta x_{\text{v}} - K_{\text{C}} \Delta P_{\text{L}}, \tag{5}$$

where the flow and flow-pressure coefficients are:

$$K_{\mathrm{Q}} = \begin{cases} \frac{c_{\mathrm{v}}}{\sqrt{2}}\sqrt{P_{\mathrm{S}} - P_{\mathrm{T}} + P_{\mathrm{L}}}, & \text{for } x_{\mathrm{v}} < 0 \\ \frac{c_{\mathrm{v}}}{\sqrt{2}}\sqrt{P_{\mathrm{S}} - P_{\mathrm{T}} - P_{\mathrm{L}}}, & \text{for } x_{\mathrm{v}} > 0 \end{cases} \tag{6a}$$

$$K_{\mathrm{C}} = \begin{cases} \frac{-c_{\mathrm{v}} x_{\mathrm{v_o}}}{2\sqrt{2}\sqrt{P_{\mathrm{S}} - P_{\mathrm{T}} + P_{\mathrm{L}}}}, & \text{for } x_{\mathrm{v}} < 0 \\ \frac{c_{\mathrm{v}} x_{\mathrm{v_o}}}{2\sqrt{2}\sqrt{P_{\mathrm{S}} - P_{\mathrm{T}} - P_{\mathrm{L}}}}, & \text{for } x_{\mathrm{v}} > 0. \end{cases} \tag{6b}$$

Although these flow and flow-pressure coefficients vary with operating conditions, for the linear analysis herein these are assumed to be constant and are evaluated from the valve's data sheet [48].

Assuming valve orifices are symmetric, matched, and under constant supply pressure, the linearized flow equation can be written as [1]:

$$\begin{aligned} Q_{\mathrm{A}} &= K_{\mathrm{Q}} x_{\mathrm{v}} - 2K_{\mathrm{C}} P_{\mathrm{A}}, \\ Q_{\mathrm{B}} &= K_{\mathrm{Q}} x_{\mathrm{v}} + 2K_{\mathrm{C}} P_{\mathrm{B}}. \end{aligned} \tag{7}$$

Since the load flow $Q_{\mathrm{L}} = (Q_{\mathrm{A}} + Q_{\mathrm{B}})/2$, from Equation (7), we get:

$$Q_{\mathrm{L}} = K_{\mathrm{Q}} x_{\mathrm{v}} - K_{\mathrm{C}} P_{\mathrm{L}}. \tag{8}$$

Applying the continuity equation to each of the piston chambers of the actuator yields [1]:

$$\begin{aligned} Q_{\mathrm{A}} - C_{\mathrm{ip}}(P_{\mathrm{A}} - P_{\mathrm{B}}) - C_{\mathrm{ep}} P_{\mathrm{A}} &= \frac{dV_{\mathrm{A}}}{dt} + \frac{V_{\mathrm{A}}}{\beta_{\mathrm{e}}}\frac{dP_{\mathrm{A}}}{dt}, \\ C_{\mathrm{ip}}(P_{\mathrm{A}} - P_{\mathrm{B}}) - C_{\mathrm{ep}} P_{\mathrm{B}} - Q_{\mathrm{B}} &= \frac{dV_{\mathrm{B}}}{dt} + \frac{V_{\mathrm{B}}}{\beta_{\mathrm{e}}}\frac{dP_{\mathrm{B}}}{dt}, \end{aligned} \tag{9}$$

where β_{e} corresponds to the effective bulk modulus $(\mathrm{N/m^2})$ of the servo oil that is the operating fluid, C_{ip} is the coefficient of internal leakage of the piston $(\mathrm{m^3/s/Pa})$, C_{ep} is the coefficient of external leakage of the piston $(\mathrm{m^3/s/Pa})$ and V_{A} and V_{B} are the forward and return chamber volumes $(\mathrm{m^3})$ of the actuator respectively, that are defined as:

$$\begin{aligned} V_{\mathrm{A}} &= V_{\mathrm{A0}} + A_{\mathrm{A}} x_{\mathrm{p}}, \\ V_{\mathrm{B}} &= V_{\mathrm{B0}} - A_{\mathrm{B}} x_{\mathrm{p}}, \end{aligned} \tag{10}$$

where V_{A0} and V_{B0} are the initial volumes of the chamber and x_{p} is the piston displacement. A_{A} and A_{B} in Equation (10) are the areas of the surface over which the pressure acts. Since the actuator is symmetric, $A_{\mathrm{A}} = A_{\mathrm{B}} \equiv A_{\mathrm{p}}$ and $V_{\mathrm{A0}} = V_{\mathrm{B0}} \equiv V_0$, and hence the total volume of the chamber becomes: $V_{\mathrm{t}} = V_{\mathrm{A}} + V_{\mathrm{B}} \equiv 2V_0$.

Solving Equations (9 and 10), and applying a Laplace transformation to the obtained equation, we get:

$$Q_{\mathrm{L}}(s) = A_{\mathrm{p}} s x_{\mathrm{p}} + C_{\mathrm{tp}} P_{\mathrm{L}} + \frac{V_{\mathrm{t}}}{4\beta_{\mathrm{e}}} s P_{\mathrm{L}}. \tag{11}$$

where, $C_{\mathrm{tp}} = C_{\mathrm{ip}} + C_{\mathrm{ep}}/2$ is the total leakage coefficient of the piston-cylinder arrangement.

Having described the flow and pressure in the actuator that results in motion of the piston, we now turn our attention to describing the dynamics of the piston.

3.1.3. Dynamics of the Piston-Cylinder

The piston applies a load on the rigid block that is assumed to not influence the system characteristics. The piston can hence be thought of as a spring, mass, and damper system that translates due to the force generated by the pressure difference across the actuator chamber plates [2]. Since the piston moves inside a fluid, it also overcomes the velocity-dependent viscous friction, which can be modelled as negative damping in the system. Though there is Coulomb friction and static friction between the piston's seals and the actuator casing, those are assumed to be velocity

independent, and are addressed in the static force analysis discussed in Section 4. Considering the viscous friction in the piston, the governing equation of motion becomes:

$$\begin{aligned} F_{\mathrm{p}} = P_{\mathrm{L}}A_{\mathrm{p}} \equiv Ms^2x_{\mathrm{p}} + (C' - K_{\mathrm{f}})sx_{\mathrm{p}} + K_{\mathrm{L}}x_{\mathrm{p}} + F_{\mathrm{L}}, \\ F_{\mathrm{p}}(s) = Ms^2x_{\mathrm{p}} + Csx_{\mathrm{p}} + K_Lx_{\mathrm{p}} + F_L, \end{aligned} \tag{12}$$

where F_{p} is the actuator force, F_{L} is the external load on the piston, M is the total translating mass (including the mass of the load cell, the mass of the piston, and of the oil translating along with the piston rod), K_{f} is the viscous coefficient of friction, C' is viscous damping coefficient of the piston, C is the net viscous damping coefficient (including the viscous coefficient of friction), and K_{L} is the overall stiffness of the piston along with the load cell. Under no external load, Equation (12) can be rewritten as a transfer function between the actuator force and the piston displacement as:

$$G_{\mathrm{piston}} = \frac{F_{\mathrm{p}}}{x_{\mathrm{p}}}(s) \equiv Ms^2 + Cs + K_{\mathrm{L}}. \tag{13}$$

3.1.4. Dynamics of the Actuator

The dynamics of the actuator are obtained by simultaneously solving Equations (8, 11, and 12) to give:

$$x_{\mathrm{p}}(s) = \frac{\frac{K_{\mathrm{Q}}x_{\mathrm{v}}(s)}{A_{\mathrm{p}}} - \frac{K_{\mathrm{Ct}}}{A_{\mathrm{p}}^2}\left(1 + \frac{V_{\mathrm{t}}}{4\beta_{\mathrm{e}}K_{\mathrm{Ct}}}s\right)F_{\mathrm{L}}}{\left(\frac{s^2}{\omega_{\mathrm{h}}^2} + \frac{2\delta_{\mathrm{h}}}{\omega_{\mathrm{h}}}s + 1\right)s + \left(\frac{CK_{\mathrm{Ct}}}{A_{\mathrm{p}}^2} + \frac{V_{\mathrm{t}}K_{\mathrm{L}}}{4\beta_{\mathrm{e}}A_{\mathrm{p}}^2}\right)s + \frac{K_{\mathrm{Ct}}K_{\mathrm{L}}}{A_{\mathrm{p}}^2}}, \tag{14}$$

where $K_{\mathrm{Ct}} = K_{\mathrm{C}} + C_{\mathrm{tp}}$ is the net flow-pressure coefficient, $\omega_{\mathrm{h}} = \sqrt{\frac{4\beta_{\mathrm{e}}A_{\mathrm{p}}^2}{MV_{\mathrm{t}}}}$ is the hydro-mechanical natural frequency (rad/s) of the system and $\delta_{\mathrm{h}} = \frac{K_{\mathrm{Ct}}}{A_{\mathrm{p}}}\sqrt{\frac{\beta_{\mathrm{e}}M}{V_{\mathrm{t}}}} + \frac{C}{4A_{\mathrm{p}}}\sqrt{\frac{V_{\mathrm{t}}}{\beta_{\mathrm{e}}M}}$ is the apparent damping ratio of the electro-hydraulic actuator. Assuming $\frac{CK_{\mathrm{Ct}}}{A_{\mathrm{p}}^2} \ll 1$ and under no external loads, Equation (14) can be reduced to obtain the transfer function between the actuator piston displacement to the valve spool displacement [1]:

$$G_{\mathrm{act}} = \frac{x_{\mathrm{p}}}{x_{\mathrm{v}}}(s) \equiv \frac{K_{\mathrm{Q}}/A_{\mathrm{p}}}{\left(\frac{s^2}{\omega_{\mathrm{h}}^2} + \frac{2\delta_{\mathrm{h}}}{\omega_{\mathrm{h}}}s + 1\right)\left(s + \frac{K_{\mathrm{Ct}}K_{\mathrm{L}}}{A_{\mathrm{p}}^2}\right)}. \tag{15}$$

Multiplying Equation (1) and Equation (15) together yields the transfer function between the voltage to the servo valve and the piston's displacement:

$$G_{\mathrm{EHA}} = G_{\mathrm{valve}}G_{\mathrm{act}} \equiv \frac{x_{\mathrm{p}}}{v}(s). \tag{16}$$

Since we are interested in knowing the dynamic force behavior as a function of the input voltage to the servo valve, Equation (13) can be combined with Equation (16) to result in the overall open-loop transfer function of the electro-hydraulic actuator:

$$G_{\mathrm{force,modelled}} = G_{\mathrm{EHA}}G_{\mathrm{piston}} \equiv \frac{F_{\mathrm{p}}}{v}(s) \equiv \frac{\left(\frac{K_{\mathrm{v}}K_{\mathrm{Q}}}{A_{\mathrm{p}}}\right)(Ms^2 + Cs + K_{\mathrm{L}})}{\left(\frac{s^2}{\omega_{\mathrm{nv}}^2} + \frac{2\zeta}{\omega_{\mathrm{nv}}}s + 1\right)\left(\frac{s^2}{\omega_{\mathrm{h}}^2} + \frac{2\delta_{\mathrm{h}}}{\omega_{\mathrm{h}}}s + 1\right)\left(s + \frac{K_{\mathrm{Ct}}K_{\mathrm{L}}}{A_{\mathrm{p}}^2}\right)}. \tag{17}$$

As is evident from Equation (17), the dynamics of the actuator are a function of the servo valve and the hydro-mechanical system. Prior to contrasting model-based dynamic behavior with experiments, the static model is discussed below.

3.2. Static Force Model of the Actuator

The actuator can apply static forces in two ways. The first is through supplying a constant DC voltage to the servo valve, and the other is by regulating the pressure in the rear chamber. These forces can also be applied together. Models for both methods are discussed separately.

3.2.1. Static Force Obtained by Actuating the Servo Valve

Since the servo valve responds to a DC voltage input, and since flow through the valve and the actuator follows the same principles as described for the case of the dynamic model, the static force model for the servo valve controlled actuator can be obtained by simply ignoring the frequency dependent terms in Equation (17), i.e., by putting $s = 0$ in Equation (17), and rearranging it, the dynamic force model reduces to a static one:

$$F_{\mathrm{s}} = \frac{vK_{\mathrm{v}}K_{\mathrm{Q}}A_{\mathrm{p}}}{K_{\mathrm{Ct}}}, \tag{18}$$

where F_{s} is the static force, and all other terms are the same as described in Section 3.1. Clearly, the static force model suggests that the force output by the servo valve controlled actuator is a function of the net flow-pressure coefficient (K_{Ct}), the flow coefficient of servo valve (K_{Q}), the piston area, and the voltage (v), and that the dependence is linear.

3.2.2. Static Force Obtained by Controlling Pressure in the Rear Chamber

The force applied by the actuator for when it is controlled by supplying fluid to the rear chamber is simply a function of the pressure in the rear chamber (P_{r}) and the area of the piston (A_{r}) in the rear chamber, which, as is evident in the schematic in Figure 1, is different than the main piston controlled by the servo valve. The pressure in the rear-chamber is governed by the pressure reducing valve. Assuming the servo valve to be turned off, the resulting force F_{r} due to the rear chamber is:

$$F_{\mathrm{r}} = P_{\mathrm{r}}A_{\mathrm{r}}. \tag{19}$$

As is evident from Equation (19), this force too is linearly dependent on the pressure and on the area of the piston. These static forces obtained from controlling the servo valve and obtained from controlling pressure in the rear chamber can be superposed (F_{s}+F_{r}) to obtain higher forces, as necessary. Having described the linearized static and dynamic force models, these are contrasted with experiments in Section 4 (static characterization) and in Section 5 (dynamic characterization).

4. Static Force Characterization of the Electro-Hydraulic Actuator

This section first discusses the static behavior controlled by the servo valve followed by the static behavior controlled by the pressure in the rear chamber. This is followed by characterizing the superposed static behavior with flow controlled with the servo valve and with pressurized fluid being supplied to the rear chamber. In each case, experiments exhibit nonlinearities, and hence the linearized static models presented in Section 3 are expanded herein to include nonlinearities.

4.1. Static Force Characterization of Actuator with Flow Control via Servo Valve

Experiments were conducted at different levels of voltages and supply pressures to understand the dependence of force on these parameters. Input voltage was varied from 0 to 2.5 V in steps of ~0.05 V, and the supply pressure was varied from 10 to 20 MPa in steps of 2 MPa. For each supply pressure, the voltage was first increased in steps until the forces stabilize and then decreased until the forces reduce to zero. An example of how the forces change with an increase in voltage for a supply pressure of 18 MPa is shown in Figure 4a and changing force characteristics with changes in voltages and pressures are summarized in Figure 4b. These experiments were all conducted with no fluid being supplied to the rear chamber.

Figure 4b also shows the model predicted forces using the linearized static force model discussed in Section 3.2.1. For model predictions, the servo valve gain, K_{v} was calculated to be 6.25×10^{-4}

m/V, the valve flow coefficient, K_Q was calculated to be 5.328 m^2/s, and the area of the piston, A_p was estimated from the computer-aided design (CAD) model of the actuator to be 2.364×10^{-4} m^2. For the linearized static force model, if we ignore the leakages in piston-cylinder arrangement, the net flow-pressure coefficient, K_{Ct} is replaced by K_C–the flow-pressure coefficient of the servo valve, which was evaluated from the flow-pressure curve for a differential pressure of 7–21 MPa [12], and was taken to be 1.6585×10^{-11} $m^3/s/Pa$. The servo valve gain, the valve flow coefficient, and the flow-pressure coefficient were all evaluated from the valve manufacturer's data sheet [48].

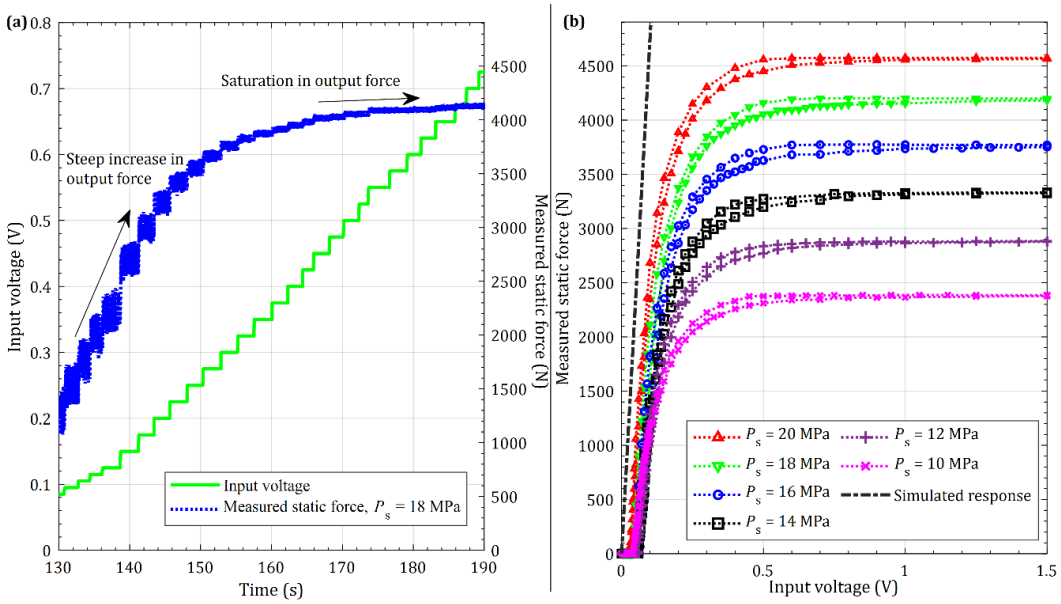

Figure 4. (**a**) Variations in static force with input voltage at a supply pressure of 18 MPa, and (**b**) measured force characteristics for changing levels of voltages and supply pressures compared with linear model-predicted forces changing with voltages.

As is evident from Figure 4a, forces increase with increasing voltages, and then saturate, i.e., when forces reach their saturation limits, a further increase in the voltage does not increase the force. Figure 4a only shows representative results for a fixed supply pressure of 18 MPa and for the forward path, and as is evident from Figure 4b which summarizes results for other pressures, and also for the reverse path—the force characteristics are similar to the case shown in Figure 4a, i.e., forces always saturate. As is also amply evident from the comparisons in Figure 4b, the linearized static force model cannot capture the measured behavior. The model suggests a linear relationship between the force and the voltage with the coefficients contributing to the slope. The model also is not dependent on the supply pressure. Experiments on the other hand suggest that forces change with supply pressure, and that forces are nonlinearly dependent on the supply voltage. Experiments also suggest that there is a certain threshold voltage that must be reached before the actuator applies a force, and that forces saturate after a certain other threshold voltage is reached. Experiments further demonstrate hysteresis in the measured forces changing with increasing and decreasing levels of voltages. All these observations clearly demonstrate that the linearized static model is inadequate.

The observed dead band region, i.e., the threshold voltage that must be reached before the actuator applies a force may be attributed to servo valve behavior [1,2,21,24], and also potentially due to the static friction that needs to be overcome [1,2,21,23,25,26]. The nonlinear force-voltage characteristics and their dependence on supply pressure may be attributed to the nonlinear characteristics of the flow-pressure coefficient [1,2], and to the leakages across the piston, and across the relief valve [1,2,23,24,27–31], and also to the nonlinear Coulombic and viscous friction behavior [1,2,23,25–29,32–36]. The observed hysteresis is also attributable to frictional hysteresis of the actuator [23], and to a lesser extent, to the electrical hysteresis caused by the inductance of the torque motor

in the servo valve [1,2,21–23], and to yet a lesser extent due to temperature related effects that change the viscosity and the bulk modulus of the oil in use [2,25,37]. The nonlinear saturation behavior is attributable to the saturation of the servo valve and the actuator [1,2,23,27,39,40]. Though some of the above observed nonlinearities have been characterized separately using models and/or experiments for the use of electro-hydraulic actuators across other engineering domains, there appears no report characterizing the cumulative influence of these nonlinearities, and none whatsoever in the context of electro-hydraulic actuators for use in machine tool structural testing applications. Each of the observed nonlinearities is included in an expanded static model—as is described next.

4.2. Modelling of Nonlinearities in the Static Force Model for Flow Control via Servo Valve

This section expands the linear static model to include nonlinearities due to flow, due to leakages and pressure drops, due to saturation, and due to friction and frictional hysteresis. Each of these effects is characterized in separate subsections as follows.

4.2.1. Nonlinearities Due to Flow and Leakages

The linear static model (see Equation (18)) suggests a linear relationship between the output force and the input voltage, with the flow coefficient (K_{Q}) and the flow-pressure coefficient (K_{C}) contributing to the slope. These coefficients, though nonlinear (see Equation (6)), were linearized assuming that they do not change with operating conditions. However, since the static characteristics evident in Figure 4 clearly exhibit nonlinearities, the dependence of these coefficients on operating parameters must be accounted for. Since the flow coefficient depends on the spool displacements (see Equations (6, 7, and 8)), which does not change much for static experiments, the flow coefficient can be assumed to remain constant. The flow-pressure coefficient on the other hand is a function of the load pressure. This dependence is valve specific and is usually described by valve manufacturers' in terms of variations in the valve flow (Q) with the pressure differential (P_{d}) across the servo valve. In the present case, we characterize this relationship by fitting a curve to the data provided by the valve manufacturer [48]. The data and the fitted relationship in logarithmic scales are shown in Figure 5.

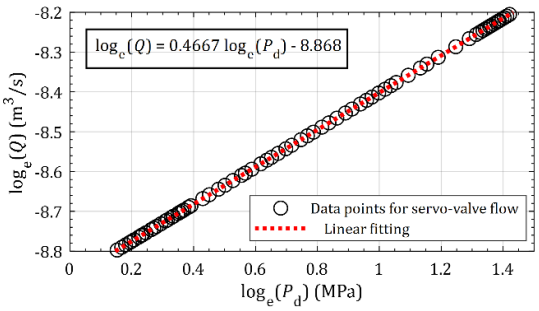

Figure 5. Variations in the valve flow (Q) with the pressure differential (P_{d}) across the servo valve.

Because of the logarithmic nature of the plot, the relationship between Q and P_{d} appears linear, when in fact an exponential fit characterizes the relationship as:

$$Q = 1.4075 \times 10^{-4} \, (P_{\mathrm{d}})^{0.4667} [\mathrm{m}^3/\mathrm{s}], \tag{20}$$

where P_{d} is in MPa. Using the Equation (20) and Equation (4) and taking into account the unit conversion of P_{d} into Pa, the nonlinear flow-pressure coefficient, denoted by $K_{\mathrm{C_{nl}}}$, can be calculated as follows:

$$K_{\mathrm{C_{nl}}} = \frac{dQ}{dP_d} \equiv 1.0407 \times 10^{-7} (P_{\mathrm{d}})^{-0.5333} \left[\frac{\mathrm{m}^3}{\mathrm{s\ Pa}}\right]. \tag{21}$$

Equation (21) clearly shows the flow-pressure coefficient to be a nonlinear function of the pressure differential across the valve. This pressure differential, in the absence of leakages, is equal

to the difference of supply pressure on the input end and the load pressure on the output end of the servo valve. However, since leakages are inadvertently present in any hydro-mechanical system, we account for them by considering leakages from the pressure relief valve, leakages in the return line, and internal leakages across the two chambers of the actuator piston. Since leakages from the relief valve feed into the main supply line leading to the servo valve, these leakages might additively contribute to the input supply pressure, and we denote this pressure by P_{o}. The leakages in the return line result in a pressure drop across the servo valve equal to the tank pressure (denoted by P_{T}). The internal leakages also result in a pressure drop, but across the piston chambers. This pressure drop is proportional to the differential pressure across the piston chambers and is here denoted by P_{in}. Accounting for these leakages, the resultant pressure differential across the valve becomes:

$$P_{\mathrm{d}} = P_{\mathrm{s}} - P_{\mathrm{L}} - P_{\mathrm{T}} + P_{\mathrm{o}}. \tag{22}$$

where P_{s} remains the supply pressure. Substituting this expression for the pressure differential within Equation (21), the flow-pressure coefficient can be rewritten as:

$$K_{\mathrm{C_{nl}}} = 1.0407 \times 10^{-7} \left(P_{\mathrm{s}} - P_{\mathrm{L}} - P_{\mathrm{T}} + P_{\mathrm{o}}\right)^{-0.5333} \left[\frac{\mathrm{m}^3}{\mathrm{s\ Pa}}\right]. \tag{23}$$

Having accounted for nonlinearities due to the servo-valve characteristics and pressure drops due to leakages, we next discuss characterization of saturation of the force.

4.2.2. Characterizing the Saturation of the Force Response

Saturation in the actuator response occurs when the load pressure achieves its limiting value of the supply pressure. Noting the linear dependence of static force (F_{s}) on the load pressure (P_{L}), the inverse relation between the slope of F/v curve and $K_{\mathrm{C_{nl}}}$ from the static force model presented in Section 3.2 and the hyperbolic relation between $K_{\mathrm{C_{nl}}}$ and the load pressure (P_{L}) as shown in Equation (23), it is easy to deduce that as the static force and hence the load pressure increases with the input voltage, so does the value of $K_{\mathrm{C_{nl}}}$ resulting in a corresponding decrease in the slope of F/v curve. As the load pressure (P_{L}) converges to its limiting value of supply pressure (P_{s}), the slope tends to zero and a constant force value is achieved, which is termed as the *Saturated Force* (F_{sat}). The voltage value at this saturation point is correspondingly termed as the *Saturation Voltage* (v_{sat}). Beyond the *Saturation Voltage* (v_{sat}), the static force is constant and independent of the input voltage. Hence, the net saturated force (F_{sat}) can be expressed using the Pascal's law as the product of the saturated load pressure ($P_{\mathrm{L,sat}}$) and the area of the central annulus of the piston, while also accounting for the pressure drop due to internal leakages across the piston chambers (P_{in}) as follows:

$$P_{\mathrm{in}} \propto P_{\mathrm{L}} \rightarrow P_{\mathrm{in}} = C_{\mathrm{in}} P_{\mathrm{L}} \tag{24}$$

where C_{in} is a cumulative coefficient of internal leakages. External leakages in the piston-cylinder assembly are neglected in the present analysis. At the saturated condition, $P_{\mathrm{L}} = P_{\mathrm{L,sat}} \equiv P_{\mathrm{s}} + P_{\mathrm{o}} - P_{\mathrm{T}}$; and hence, $P_{\mathrm{in,sat}} = C_{\mathrm{in}} P_{\mathrm{L,sat}}$, which makes the saturation force to be:

$$F_{\mathrm{sat}} = \left(P_{\mathrm{L,sat}} - P_{\mathrm{in,sat}}\right) A_{\mathrm{P}} \equiv P_{\mathrm{L,sat}} (1 - C_{\mathrm{in}}) A_{\mathrm{P}}, \tag{25}$$

Equation (25) can be rewritten in a more convenient form as:

$$F_{\mathrm{sat}} = (P_{\mathrm{s}} + P_{\mathrm{o}} - P_{\mathrm{T}})(1 - C_{\mathrm{in}}) A_{\mathrm{P}} \equiv P_{\mathrm{s}} (1 - C_{\mathrm{in}}) A_{\mathrm{P}} + (P_{\mathrm{o}} - P_{\mathrm{T}})(1 - C_{\mathrm{in}}) A_{\mathrm{P}}. \tag{26}$$

This re-arrangement suggests that the slope of the relationship between F_{sat} and P_{s} must be equal to $(1 - C_{\mathrm{in}}) A_{\mathrm{P}}$, and the intercept must be equal to $(P_{\mathrm{o}} - P_{\mathrm{T}})(1 - C_{\mathrm{in}}) A_{\mathrm{p}}$. Since A_{p} is a design parameter and is known beforehand, and the tank pressure P_{T} can be taken to be the atmospheric pressure (1 atm), the coefficient of internal leakages, C_{in} and the pressure leakage from the pressure reducing valve, P_{o} can be easily estimated by fitting a line to the measured relationship between F_{sat} and P_{s} based on the characteristic behavior in Figure 4. The resulting linear fit is shown in Figure 6.

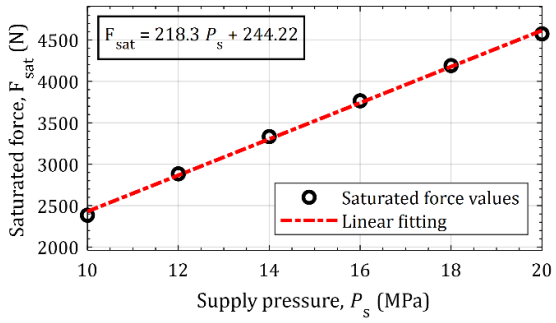

Figure 6. Linear fit of saturated force values as a function of the supply pressure.

Using the linear fit equation in conjunction with Equation (26), the coefficient of internal leakage and the pressure leakage form the pressure reducing valve can be identified to be $C_{\text{in}} = 0.0680$ and $P_{\text{o}} = 1.1157$ MPa respectively.

Having characterized the saturated force behavior and having systematically identified the unknown model parameters including the flow coefficients, leakage coefficients and the pressure drops, we re-define the static force model (Equation (18)) as:

$$\frac{F_{\text{s}}}{v} = \frac{K_{\text{v}} K_{\text{Q}} A_{\text{p}} (1 - C_{\text{in}})}{1.0407 \times 10^{-7} \, (P_{\text{s}} - P_{\text{L}} - P_{\text{T}} + P_{\text{o}})^{-0.5333}} \equiv \frac{K_{\text{v}} K_{\text{Q}}}{K_{\text{C}}'} A_{\text{p}} (1 - C_{\text{in}}) (P_{\text{s}} - P_{\text{L}} - P_{\text{T}} + P_{\text{o}})^{0.5333}, \tag{27}$$

where $K_{\text{C}}' = 1.0407 \times 10^{-7}$ is a constant value.

Having characterized the nonlinearities which directly influence the force generation within the system, we next discuss frictional nonlinearities that are external to the source of force application but still influence the static force characteristics and contribute to the hysteresis in the system.

4.2.3. Nonlinearities Due to Friction and Frictional Hysteresis

To better understand the influence of frictional nonlinearities on the static force response of the system, consider the partitioning of force–voltage behavior for a representative supply pressure of 20 MPa into the four regions as shown in Figure 7. These four regions are classified as the no-force region, the linear region, the transition region, and the saturation region.

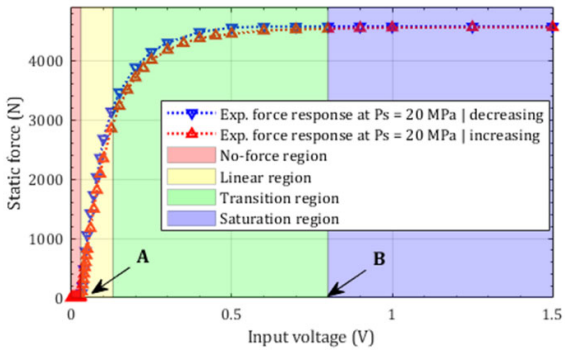

Figure 7. Classification of the measured force-voltage characteristics into four distinct regions.

As is evident from Figure 7, in the no-force region, even as the voltage is increased, there is no force until point 'A' is reached (denoted by the *Onset Voltage*). This suggests that for the piston to move and exert a force, it must overcome some static friction, and hence this region must be characterized by a static friction model. As the voltage is increased beyond the point 'A', the piston breaks away the static friction and starts to slide, and consequently the output force increases. The linear increase in the static force is bounded by the Coulombic friction force and hence, the Coulombic

friction model defines the friction behavior in the linear region. The transition region defines the transition from the linear force profile to the start of the force saturation region, i.e., point 'B'. The slope of the force-voltage plot slowly tends towards zero, and so does the velocity of the piston. As the velocity tends to zero, the friction value goes below the maximum friction defined by the Coulombic friction model, and the viscous friction model comes into action. Hence, the friction in this nonlinear steady transition region is possibly governed by a viscous friction model. Since the viscous friction has a strong dependence on the piston velocity, it plays a major role in the frictional hysteresis—which appears to be dominant only in the transition region—see Figure 7. Beyond point 'B', which marks the *Saturation Voltage*, the force saturates suggesting that the piston velocity becomes zero, and since there is no relative motion, friction plays no role in the saturation region.

The characteristic behavior of the static force suggests that the frictional effects can be modelled by a static friction model in the 'no-force' region, by a Coulombic friction model in the linear region, and by a viscous friction model in the transition region. These models are formulated as under.

- Static friction model:

The static frictional force, F_{sf} that must be overcome for the piston to slide and for the actuator to apply a force can be characterized by:

$$F_{sf} = \begin{cases} +F_s & \text{for } \dot{x}_p = 0, F_s < F_{sf,max} \text{ and a tendency of forward sliding} \\ -F_s & \text{for } \dot{x}_p = 0, F_s < F_{sf,max} \text{ and a tendency of backward sliding} \end{cases} \quad (28)$$

where $F_{sf,max}$ is the maximum static friction value, $\dot{x}_p$ denotes the piston velocity, and F_s is the output static force of the actuator. This static frictional force was estimated using the setup as shown in Figure 8. As shown, the actuator was placed with the piston facing upwards, and different calibrated weights were placed incrementally on the piston, and the weight under which the piston moved downwards was recorded as the weight which equates the static frictional force. The static frictional force was hence experimentally calibrated to be ~44 N.

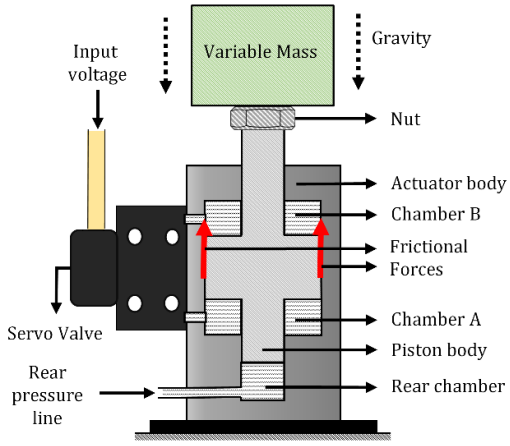

Figure 8. Schematic of the experimental setup to calibrate the static frictional force.

- Coulomb friction model:

The frictional force behavior in the linear region is characterized by the Coulomb friction model which suggests the friction force to be a constant beyond the threshold value of maximum Coulombic friction as follows:

$$F_{cf} = F_{cf,max} \operatorname{sign}(\dot{x}_p), \quad \text{for } \dot{x}_p \neq 0 \text{ and } F_s > F_{cf,max}, \quad (29)$$

where F_{cf} denotes the Coulombic frictional force, $F_{cf,max}$ denotes the maximum Coulomb sliding friction value, and F_s denotes the output static force. The value of $F_{cf,max}$ is found experimentally

using similar methodology as reported in [23,32]. The piston was manually pulled via a digital force gauge (Make: Eagle, Model number: EEL6001A), and the corresponding pull force, just sufficient to make the piston slide, was recorded. Three sets of experiments were carried out and an average pull force value of ~39 N was taken as the maximum Coulomb sliding friction value, $F_{\mathrm{cf,max}}$.

- Viscous friction model:

To characterize the frictional behavior in the transition region, the piston-velocity dependent viscous friction model is considered:

$$F_{\mathrm{vf}}(t) = K_{\mathrm{f}}\,\dot{x}_{\mathrm{P}}(t), \tag{30}$$

where in $F_{\mathrm{vf}}(t)$ denotes the viscous friction force, and K_{f} is the same viscous coefficient of friction as described in Equation (12). Since this coefficient is to be calibrated through experiments, and since we do not explicitly measure the velocity of the piston, we instead rewrite the viscous friction force to be dependent on the change in the force with voltage. To do so, we rewrite the static force in Equation (12) under no external load (i.e., $F_{\mathrm{s}} = K_{\mathrm{L}}x_{\mathrm{p}}$,) to change with voltage as:

$$\frac{dF_{\mathrm{s}}}{dv} = K_{\mathrm{L}}\frac{dx_{\mathrm{p}}}{dv} \tag{31}$$

where K_{L} is the overall stiffness of the piston along with the load cell, and x_{p} is the position of the piston. Since experiments involve ramping the input voltage (at a constant slope) with time, hence, the time derivative of voltage comes out to be the constant slope value from which we get the time derivative of the piston displacement in terms of the output force as follows:

$$\frac{dF_{\mathrm{s}}}{dv} = K_{\mathrm{L}}\frac{dx_{\mathrm{p}}}{dt}\frac{dt}{dv} = \frac{K_{\mathrm{L}}}{K_{\mathrm{v/t}}}\frac{dx_p}{dt} \rightarrow \frac{dx_{\mathrm{p}}}{dt} = \frac{K_{\mathrm{v/t}}}{K_{\mathrm{L}}}\frac{dF_{\mathrm{s}}}{dv} \tag{32}$$

where in $K_{\mathrm{v/t}}$ is the slope of the ramped input voltage and hence, a model-dependent factor. Since, for a simulation time of 10 s, the voltage signal was ramped from 0 to 2.5 V and back from 2.5 to 0 V, hence, the slope value which gives the time derivative of the voltage signal ($K_{\mathrm{v/t}}$), was calculated to be 0.5 V/s for increasing force values and −0.5 V/s for decreasing force values. Now, substituting Equation (32) into Equation (30), we get the modified viscous friction model as:

$$F_{\mathrm{vf}}(t) = K_{\mathrm{f}}\,\dot{x}_{\mathrm{p}}(t) = \frac{K_{\mathrm{f}}\,K_{\mathrm{v/t}}}{K_{\mathrm{L}}}\left(\frac{dF_{\mathrm{s}}}{dv}\right) = C_{\mathrm{vf}}\frac{dF_{\mathrm{s}}}{dv} \tag{33}$$

where C_{vf} is defined as the cumulative coefficient of viscous friction, which can be calibrated to fit the observed behavior in the transition region. The calibrated cumulative coefficient of viscous friction was found to be 0.2 V.

Combining the static friction model, the Coulombic frictional model, and the viscous frictional model, we get the net frictional force behavior modelled as follows:

$$F_{\mathrm{f}} = \begin{cases} F_{\mathrm{sf}} & \text{for } \dot{x}_{\mathrm{P}} = 0, F_{\mathrm{s}} < F_{\mathrm{sf,max}} \\ F_{\mathrm{cf}} & \text{for } \dot{x}_{\mathrm{P}} \neq 0, F_{\mathrm{s}} > F_{\mathrm{cf,max}} \\ F_{\mathrm{vf}}(t) & \text{for } \dot{x}_{\mathrm{P}} \neq 0, F_{\mathrm{s}} \leq F_{\mathrm{cf,max}} \end{cases} \tag{34}$$

4.2.4. Nonlinearities Due to Dead bands, Electrical Hysteresis, and the Effect of Temperature

The no-force region of the force-voltage curve shown in Figure 7 is generally caused by the combined effects of the static friction, spool overlaps and zero offsets in the spool of the servo valve. Static frictional effects have already been accounted for as discussed in Section 4.2.3, and since the valve under use has a critically centered spool and the zero offsets specified in the valve datasheet are less than 1%, their influence is expected to be negligible. Similarly, for the servo valve under use, the specified electrical hysteresis as per the valve datasheet is also less than 1.5% over the operating range of the system, and its effect is also expected to be negligible. Though negligible, the effects of

spool overlaps, zero offsets, and electrical hysteresis are accounted for by introducing an '*Offset Voltage*' in the model, which is estimated to be ~1.5% of the operating voltage range, i.e., 0.0375 V.

Although temperature is not a control parameter of the system, to understand its influence on the force, experiments were performed with the system kept in continuous operation at a supply pressure of 20 MPa, with the oil temperature of the hydraulic tank and the force applied being recorded at periodic intervals of 10 min. These measurements shown in Figure 9, show the forces increasing with an increase in temperature–which is consistent with trends reported in [37]. Since forces only increase by 3% for a 30 °C increase in temperature, and since all experiments for all analysis in this paper were performed only when the oil temperature was consistently between 30 °C to 50 °C, for which range the change in forces is negligible, hence, effects of temperature are ignored in this analysis.

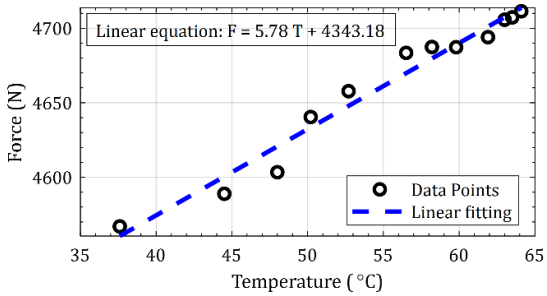

Figure 9. Measured increase in saturated forces with an increase in temperature.

Having characterized the nonlinearities due to flow and leakages, and due to friction, and having also accounted for the saturation behavior, the static model for force application by controlling the servo valve is updated to include the nonlinear characteristics—as discussed next.

4.3. Expanded Nonlinear Static Force Model Obtained by Actuating the Servo Valve

The major nonlinearities in the static response of the system were identified and modelled using a block-diagram approach using Simulink®-as shown in Figure 10. The model comprises of two sections. The section on '*Force generation and flow-pressure dynamics*' includes the model for nonlinear servo valve characteristics, pressure drops across the servo valve and internal leakages across the piston; and the section on the '*Friction model*' accounts for the influence of the friction on the static force. To mimic experimental procedures, the input voltage is ramped to increase and then, decrease. To account for the nonlinearities due to dead-bands and electrical hysteresis—as discussed in Sections 4.2.3 and in 4.2.4, an *Offset Voltage* is subtracted from the input signal—which results in a positive shift in the voltage axis of the force curve to help characterize the 'no-force' region. The 'servo flow gain' shown in Figure 10 is a product of the servo gain (K_v) and of the flow coefficient (K_Q). All other parameters shown in Figure 10 are the same as described in Section 4.2. The load pressure is recursively calculated from the output force using Pascal's law. This is achieved using a force feedback-loop as shown in Figure 10. For the friction model, the measured output force is differentiated with respect to the input voltage to compute the viscous friction force as per Equation (33), and a saturation block is used to model the Coulombic friction force. Another saturation block is used to set a lower bound on the output force as defined by the static friction model, which ensures that the output force remains zero until the threshold limit defined by the static friction is achieved.

Using the expanded nonlinear static model, force predictions for different supply pressures are compared with experimental results in Figure 11. As is amply evident, model predictions can faithfully capture all observed behavior for different supply pressures of interest. The no-force region is captured well, as is the nonlinear transition from the linear region to the saturation region. Seeing how the expanded model accounts for nonlinearities due to flow and leakages, and due to friction and frictional hysteresis, as well as for the saturation behavior, it is reasonable to conclude that the expanded nonlinear static force model of the actuator with flow controlled with the servo valve is validated. Such systematic characterization of all major nonlinearities included in a single expanded static model for

electro-hydraulic actuators is a new contribution to the literature on modelling, characterizing, and understating the nonlinear behavior of servo valve controlled electro-hydraulic actuators.

Similar analysis as was presented herein for flow controlled by the servo valve is presented in the next section to characterize the static force obtained by controlling pressure in the rear chamber.

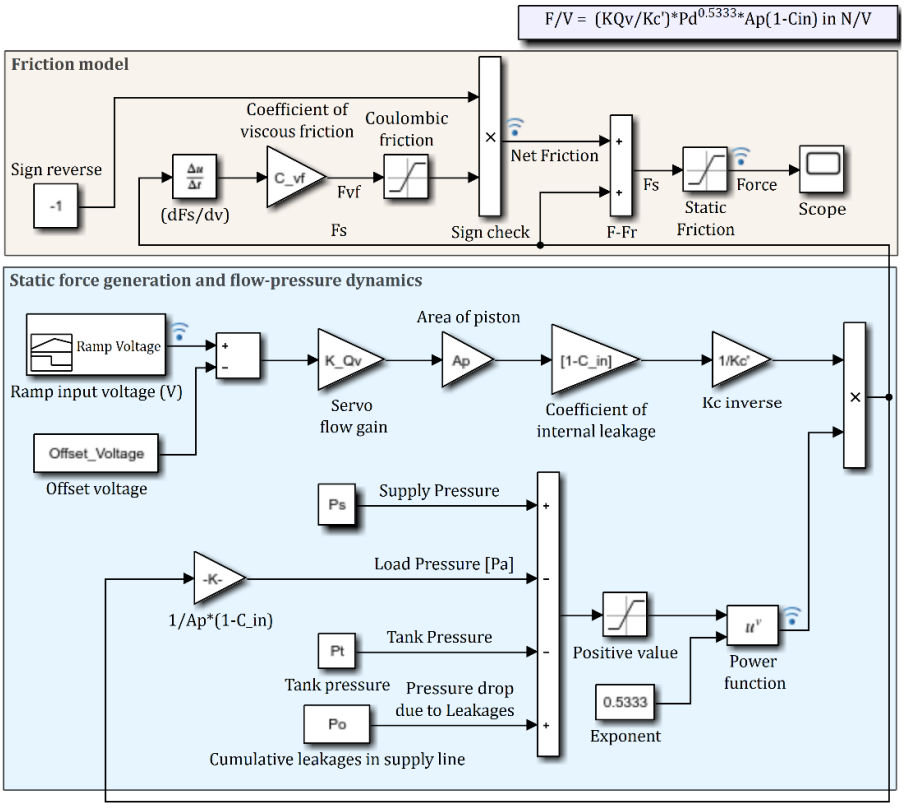

Figure 10. Simulink block diagram of the nonlinear static force model of the actuator with flow controlled with servo valve.

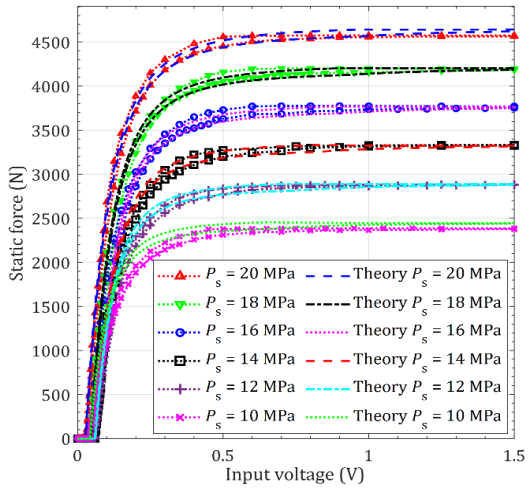

Figure 11. Comparison of the measured and theoretically predicted nonlinear static force characteristics of the actuator for flow control via servo valve.

4.4. Static Force Characterization of the Actuator by Controlling Pressure in the Rear Chamber

Experiments were conducted by regulating the pressure in the rear chamber by using the pressure reducing valve. To isolate these experiments from the influence of the servo valve, the servo valve was turned off. The pressure reducing valve was used to increase the pressure in the rear chamber in steps of 1 MPa until the pressure in the rear chamber equaled the supply pressure, which was controlled independently. Two separate experiments with two different supply pressures were conducted. On reaching the saturation limit (when pressure in the rear chamber equaled the supply pressure), the pressure in the rear chamber was decreased in steps of 1 MPa. The pressure across the pressure reducing valve was monitored using a pressure gauge, and the force was measured using the same load cell. The resulting measured forces changing with pressures in the rear chamber are shown in Figure 12. For comparison purposes, the predicted static forces using the linear rear-force model (Equation (19)) described in Section 3.2.2 are also shown in Figure 12. For model predictions, A_r was identified from the CAD model of the actuator and was taken to be 2.544×10^{-4} m^2.

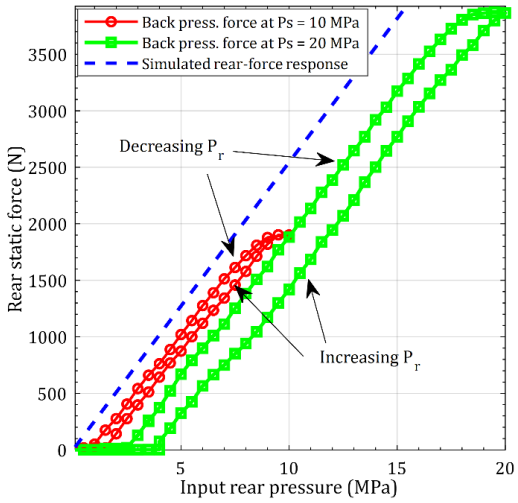

Figure 12. Comparison of model predicted forces along with measured force characteristics changing with a change in the pressure in the rear chamber for two different supply pressure settings.

As is evident from Figure 12, the measured force characteristics are very different than model predictions, and are also very different than the measured force characteristics for force applied by controlling flow to the servo valve (see Figure 4). Even though the force model for pressurized flow in the rear chamber is linear, experiments are not. The measured output force clearly saturates at pressures in the rear chamber equaling the supply pressure. Measured characteristics also suggest that there is certain threshold value of the pressure in the rear chamber that must be reached before which the actuator can exert a force. Measurements also exhibit hysteresis. Though the model predicted slope is like that of the measurements, the model is clearly inadequate, and it must hence be expanded to include the experimental observations.

The observed dead band region, i.e., the threshold pressure in the rear chamber that must be reached before the actuator applies a force may be attributed to the servo valve behavior, even when it is off, and can be explained by the accounting for the 'no-load' leakages [1,21,23,27,48]. Even when the servo valve is turned off, there is some fluid flowing into both the piston chambers and further, back to the tank via the return line. This fluid-flow at zero voltage, termed as the 'no-load' leakage in the servo valve maintains the piston chambers at a certain pressure value termed as the no-load chamber pressure (P_{ch}). The fluid in the main piston chambers A and B (see Figure 1) potentially obstructs the sliding motion of the piston, and hence may influence the force response due to pressurized flow supplied to the rear-chamber. This no-load chamber pressure was inactive in the previous static-force analysis via the servo valve, because at no load, the pressure in both the chambers are equal and hence cancel each other out. However, in the present case, the chamber

pressure is potentially responsible for resisting the motion of the piston until some threshold rear chamber pressure is achieved.

The no-load chamber pressure in that sense, acts like friction resisting motion, and may also help explain the large hysteresis that is observed, and can be explained as follows: as the piston slides ahead, the fluid in the piston chamber B (at front) is compressed and exerts an opposite pressure on the piston reducing the net force. However, during the backward motion of the piston, the fluid in the chamber A undergoes compression, and exerts a similar force but in the forward direction, thus resisting the motion of the piston. This velocity-dependent behavior is like the friction model proposed in Section 4.2.3 and may help explain the observed hysteresis. The dependence of this hysteresis behavior on the supply pressure can be attributed to the fact that the no-load chamber pressure in the servo valve is known to be proportional to the supply pressure acting on the input end of the servo valve [21,27,48]. For similar reasons, the threshold pressure that must be reached in the rear chamber before the actuator exerts a force must also be a function of the supply pressure.

Though there has been some reporting and characterization of the nonlinearities due to servo valve-controlled actuators, there appear no reports explaining and/or modelling the above described force nonlinearities due to pressurized flow in the rear chamber. Each of the observed nonlinearities are included in an expanded static model for the actuator of interest—as is described next.

4.5. Modelling of Nonlinearities in the Static Force Model for Pressurized Flow to the Rear Chamber

This section expands the static force model for force obtained by supplying pressurized flow to the rear chamber by including nonlinearities due to no-load leakages, due to friction, and due to hysteresis. Each of these nonlinearities are characterized separately in the subsections discussed next.

4.5.1. Nonlinearities Due to Leakages in the System

Three basic leakages are considered in the present analysis, namely the leakages from the pressure reducing valve in the rear pressure line, the leakages from the rear chamber of the piston, and the leakages from the servo valve to the main piston chambers. The leakages in the rear pressure line occur through the pressure reducing valve, which is connected to the high-pressure main supply line. These leakages seep into the high-pressure supply line and add to the rear pressure and are denoted by P_{PR}. The drop in pressure due to internal leakages from the rear chamber of the piston (P_{rch}) is similar to that considered across the main piston chambers in the static force analysis with the servo valve. They are, hence, similarly modelled as a linear function of the rear-pressure (P_{r}) of the actuator as follows:

$$P_{\mathrm{rch}} = C_{\mathrm{rch}}\, P_{\mathrm{r,net}} \tag{35}$$

where C_{rch} is the constant of proportionality which is equal to the coefficient of rear-chamber leakage and $P_{\mathrm{r,net}}$ denotes the net rear pressure including the leakages, as defined ahead in Equation (37).

As discussed in Section 4.4, the no-load chamber pressure acts like friction and resists the sliding motion of the piston. Thus, as the rear pressure is gradually increased, the piston tends to slide ahead, but the pressure in chamber B resists this force till a threshold value of rear pressure is reached. This threshold pressure, denoted by P_{th}, is modelled as a linear function of the supply pressure as:

$$P_{\mathrm{th}} = C_{\mathrm{th}}\, \frac{A_{\mathrm{p}}}{A_r}\, P_{\mathrm{s}} \tag{36}$$

where C_{th} is the coefficient of the threshold pressure value, A_{p} and A_{r} are the cross-sectional areas of the piston's central annulus and the rear-surface, respectively, and P_{s} is the supply pressure. Since the threshold pressure is defined in terms of the rear pressure which acts on the rear surface, and since the chamber pressure acts on the central annulus area (A_{p}), the factor $A_{\mathrm{p}}/A_{\mathrm{r}}$ is included in Equation (36) to maintain force equivalence in the system.

Including the influence of leakages in the rear chamber based static force model, we get:

$$F_{\mathrm{r}} = (P_{\mathrm{r,net}} - P_{\mathrm{rch}})A_{\mathrm{r}} \equiv (P_{\mathrm{r}} - P_{\mathrm{th}} + P_{\mathrm{PR}})(1 - C_{\mathrm{rch}})A_{\mathrm{r}} \tag{37}$$

where P_{rch} is defined in Equation (35), in which the net rear pressure, $P_{\mathrm{r,net}} = P_{\mathrm{r}} - P_{\mathrm{th}} + P_{\mathrm{PR}}$, and the threshold pressure, P_{th} is defined in Equation (36). Substituting for these, and rearranging the resulting equation in a more convenient form, we get:

$$F_{\mathrm{r}} = P_{\mathrm{r}}(1 - C_{\mathrm{rch}})A_{\mathrm{r}} + (1 - C_{\mathrm{rch}})A_{\mathrm{r}}\left(P_{\mathrm{PR}} - \left(\frac{C_{\mathrm{th}}A_{\mathrm{p}}}{A_r}\right)P_{\mathrm{s}}\right). \tag{38}$$

This force equation represents the equation for a line, and knowing A_{r} and A_{p}, the unknown C_{rch}, P_{PR} and C_{th} can be found from the measured characteristics of F_{r} vs P_{r} for different known values of P_{s}–as is shown in Figure 12. The unknowns are hence estimated as: C_{rch} = 0.03623; P_{PR} = 0.6 MPa; C_{th} = 0.184. Having thus characterized the nonlinearities due to leakages, we now turn our attention to characterizing nonlinearities due to friction and due to frictional hysteresis.

4.5.2. Nonlinearities Due to Friction and Frictional Hysteresis

The friction model developed previously in the case of static force characterization with the servo valve was largely defined by the characteristics of the piston. Since the hydraulic piston and the actuation manner remains the same, hence, the same friction model is considered here as well. Similar to the friction model discussed in Section 4.2.3, the net frictional force is defined by the combination of the static friction model, the viscous friction model and the Coulombic friction model. The parameters of the static friction model and the Coulombic friction model are piston-dependent and hence, remain the same. However, the viscous friction model is a function of the piston velocity, which was earlier (in Section 4.2.3) expressed in terms of the slope of the output force plot with the input voltage. In a similar fashion, the slope of the rear force plot with the rear pressure is used to estimate the piston velocity, as shown below:

$$F_r = K_L x_p \rightarrow \frac{dF_{\mathrm{r}}}{dP_{\mathrm{r}}} = K_{\mathrm{L}}\frac{dx_{\mathrm{p}}}{dP_{\mathrm{r}}} \equiv K_{\mathrm{L}}\frac{dx_{\mathrm{p}}}{dt}\frac{dt}{dP_{\mathrm{r}}} \equiv \frac{K_{\mathrm{L}}}{K_{\mathrm{P/t}}}\frac{dx_{\mathrm{p}}}{dt}, \tag{39}$$

where in K_{L} denotes the stiffness of the piston, and $K_{\mathrm{P/t}}$ denotes the slope of the ramped input signal, i.e., the rear chamber pressure, and is a model-dependent factor. Since the rear pressure signal was ramped from 0 to 20 MPa and back within a simulation time of 10 s, $K_{\mathrm{P/t}}$ was estimated to be 4 MPa/s. Using Equation (39), the viscous friction model becomes:

$$F_{\mathrm{vf}}(t) = K_{\mathrm{f}}\,\dot{x}_{\mathrm{P}}(t) \equiv \frac{K_{\mathrm{f}}\,K_{\mathrm{P/t}}}{K_{\mathrm{L}}}\left(\frac{dF_{\mathrm{r}}}{dv}\right) = C_{\mathrm{vf}}\frac{K_{\mathrm{P/t}}}{K_{\mathrm{v/t}}}\left(\frac{dF_{\mathrm{r}}}{dv}\right), \tag{40}$$

where in C_{vf} is the cumulative coefficient of viscous friction and is identified to be 0.2 V in Section 4.2.3.

The only modification from the friction model described in Section 4.2.3, is the change in the control parameter which was the input voltage in the case of the servo valve and is the rear pressure herein. However, both are ramped with a constant slope with respect to time, hence mathematically, both models are equivalent.

4.5.3. Hysteretic Nonlinearities Due to the No-load Chamber Pressures

Hysteresis in the system can be attributed to the no-load chamber pressure generated in the piston chambers due to leakages or no-load flow in the servo valve. Such leakages in the servo valve are proportional to the supply pressure of the system acting on the input end of the servo valve. Just like friction, the no-load chamber pressures would exert an opposite force on the piston, thus reducing the net output force in the case of forward motion of the piston, while increasing the same in the case of backward movement of the piston. Thus, the model for no-load chamber pressures should depend on the direction of motion of the piston, which can be directly related to the sliding velocity of the piston. Using the same modelling strategy as that for modelling of friction, the direction of sliding motion of the hydraulic piston is calculated and then used to determine the direction of the resistive force due to the piston chamber pressure. Based on the above discussions,

the no-load chamber pressure, P_{ch} is modelled to be proportional to the supply pressure and to the piston velocity, as:

$$P_{ch} \propto P_s, \text{and } P_{ch} \propto -\text{sign}\left(\frac{dx_p}{dt}\right) \rightarrow P_{ch} = -C_{ch}P_s \,\text{sign}\left(\frac{dx_p}{dt}\right) \tag{41}$$

where x_p denotes the piston displacement and C_{ch} is the coefficient of no-load chamber pressure. The velocity term in Equation (41) can again be replaced with the slope of the rear force plot, as described in Equation (39). Since K_L and $K_{P/t}$ are both positive quantities, therefore the sign of the displacement gradient of the hydraulic piston $\left(dx_p/dt\right)$ is same as the sign of the slope of the force curve (dF_r/dP_r), and the no-load chamber pressure can hence be rewritten as:

$$P_{ch} = -C_{ch}P_s \,\text{sign}\left(\frac{dF_r}{dP_r}\right). \tag{42}$$

The corresponding force due to the no-load chamber pressure becomes:

$$F_{ch} = -A_r C_{ch}P_s \,\text{sign}\left(\frac{dF_r}{dP_r}\right). \tag{43}$$

Since the resultant force due to the chamber pressure, as formulated above is proportional to the supply pressure, therefore, at lower supply pressure values the amount of hysteresis is low, and at higher supply pressures, the hysteresis is high. Additionally, the change in the sign of the slope of the curve changes the sign of the force as well, and hence, the ideal force curve (without hysteresis) is displaced equally about its mean position i.e., it is shifted downwards with increasing rear pressures, and shifted upwards with decreasing rear pressures. The unknown gain C_{ch} in Equation (43) is identified by equating the magnitude of hysteresis in the experimental plot (see Figure 12) for a known supply pressure value with that of the hysteresis model as in Equation (43), and it comes out to be 9×10^{-5}.

Having characterized the nonlinearities due to leakages, and due to friction, and having also accounted for hysteretic behavior, the static model for force application by controlling the pressure in the rear chamber is updated to include the nonlinear characteristics—as discussed next.

4.6. Expanded Nonlinear Static Model for Pressurized Flow Supplied to the Rear Chamber

The major nonlinearities in the static response of the system due to pressurized flow supplied to the rear chamber were identified and modelled using a block-diagram representation using Simulink®-as shown in Figure 13. The model comprises of three sections, each separately accounting for the influence of non-linearities in the three distinct components of the system, namely, the rear pressure chamber, the servo valve, and the piston.

The section on '*Rear force generation and leakages*' models the forces in the rear pressure chamber and the associated non-linearities due to leakages. Similar to the experimental procedures, the input rear pressure is modelled as a ramped signal followed by a saturation block that has an upper threshold equal to the supply pressure value to ensure that the rear pressure does not exceed the supply pressure. Leakages due to pressure reducing valve are modelled as constant pressure drops while the no-load chamber pressure is modelled as a function of the supply pressure. The section on the '*Friction model*' accounts for nonlinearities due to mechanical characteristics of piston-cylinder. The piston velocity is evaluated by the derivative of the rear force with respect to the input rear pressure. The cumulative viscous friction is modelled as a product of rear force-pressure gradient and cumulative coefficient of viscous friction. The Coulombic model is captured using a saturation block as in Section 4.3. The static friction model is also represented by a saturation block just prior to the final force output to keep a check on the lower threshold value of force output. The section on '*No-load chamber Leakages*' models the hysteretic behavior due to the no-load chamber pressure as per Equation (43). The piston velocity is evaluated as in the section on the '*Friction model*'. The signum function is implemented as shown and the leakage coefficient and the supply pressure are modelled as gains.

The algebraic sum of the rear force, the friction force, and the force due to the no-load chamber leakages, results in effective force output by supplying pressurized fluid to the rear chamber. Using this expanded nonlinear static model, force predictions for different supply pressures are compared with experimental results in Figure 14.

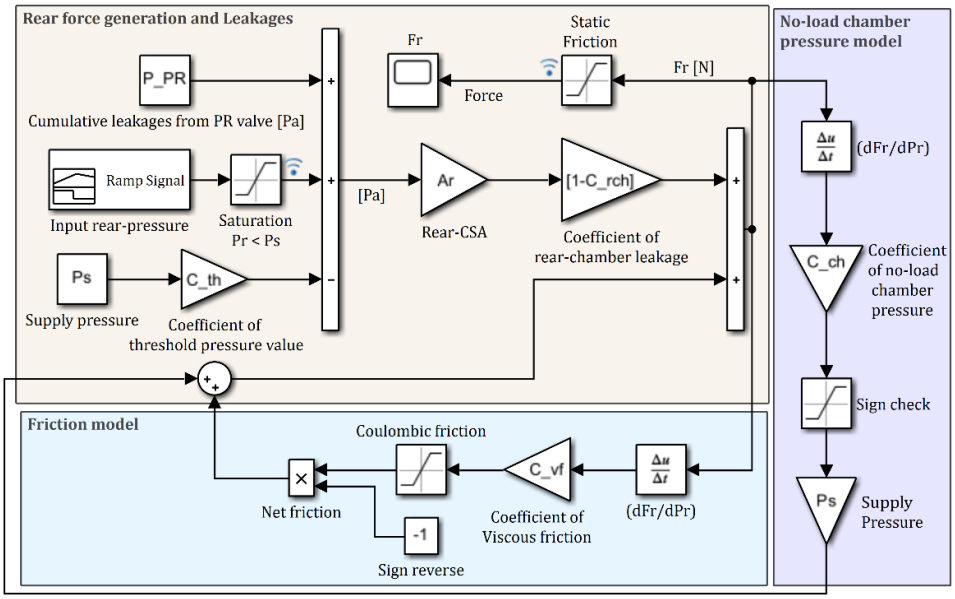

Figure 13. Simulink block diagram of the nonlinear static force model of the actuator with pressurized flow supplied to the rear chamber.

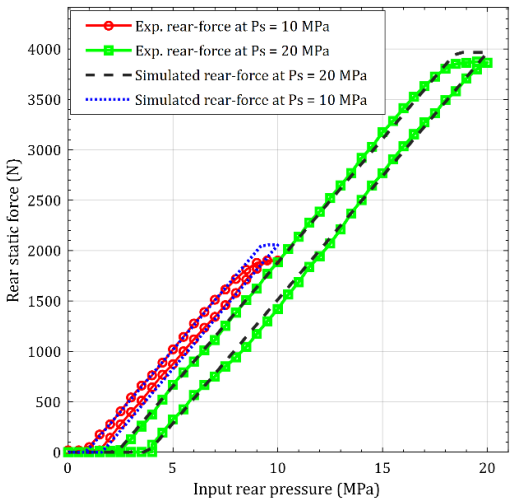

Figure 14. Comparison of the measured and theoretically predicted nonlinear static force characteristics of the actuator for pressurized flow supplied to the rear chamber.

As is amply evident from Figure 14, predictions using the expanded nonlinear static model can faithfully capture all observed behavior for different supply pressures of interest. The no-force region is captured well, as is the hysteretic behavior. Seeing how the expanded model accounts for nonlinearities due to leakages, and due to friction and frictional hysteresis, as well as for the saturation behavior, it is reasonable to conclude that the expanded nonlinear static force model of the actuator with pressurized flow supplied to the rear chamber is also validated. Such systematic

characterization of all major nonlinearities included in an expanded static force model for pressurized flow supplied to the rear chamber is a new contribution to the literature.

Seeing how the expanded nonlinear static force models for the valve-controlled actuator and for the case of pressurized fluid supplied to the rear chamber have both been validated separately, and since the actuator is designed such that the pressurized fluid in the rear chamber can be supplied over and above the flow through the servo valve such that higher forces may be applied to structure being tested, characteristic behavior for the superposition of these forces is described next.

4.7. Static Force Characteristics for Superposition of Forces Obtained from Controlling the Servo Valve and from Supplying Pressurized Flow to the Rear Chamber

To characterize the static behavior of the actuator when forces obtained from controlling the servo valve are superposed with those obtained from controlling pressure in the rear chamber, experiments were performed at different values of the rear chamber pressure and with different values of input voltages being supplied to the servo valve at a constant supply pressure of 20 MPa. For pressure in the rear chamber being 0, 2, 4 and 6 MPa, respectively, the input voltage was increased from 0 to 2.5 V and then decreased back from 2.5 to 0 V, in steps of 0.05 V for each rear pressure value. The output forces were recorded and compared with model predictions that account for all the nonlinearities characterized in Sections 4.1–4.6.

The block-diagram representation of the static model that superposes forces obtained from controlling the servo valve with those obtained from controlling pressure in the rear chamber is shown in Figure 15. Since the characterization of the valve controlled force behavior was carried out with no pressurized fluid supplied to the rear chamber in Section 4.1–4.3, and since characterization of the force behavior for pressurized flow to the rear chamber was carried out with the servo valve being turned 'off' (Section 4.4–4.6), the model in Figure 15 is a modified version of the models presented in Figures 10 and 13. For example, the characterization of the force behavior with pressurized fluid in the rear chamber with the servo valve turned 'off' accounted for the no-load chamber leakages which would not have existed had the servo valve been in operation. Since the servo valve is 'on' when things work in conjunction, the no-load leakages can be neglected as the no-load chamber pressure in both the piston chambers cancel out each other. Furthermore, since the friction model is present in both cases, and since they are essentially the same, only one friction model is retained as shown in Figure 15.

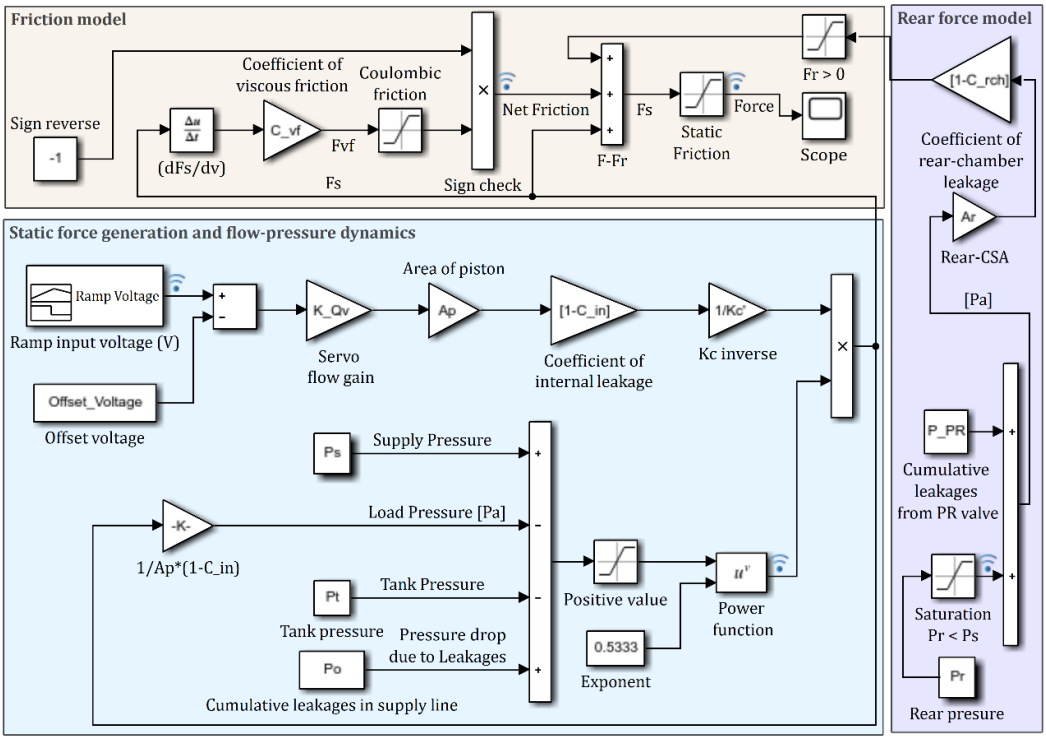

Figure 15. Simulink block diagram of the cumulative nonlinear static force model of the actuator with flow controlled with servo valve and pressurized flow supplied to the rear chamber.

The model shown in Figure 15 has three parts. The sections on '*Force generation and flow-pressure dynamics*', and the section on the '*Friction model*' are essentially the same as in Figure 10, and the section on the '*Rear force model*' essentially reduces to a rear force, with the internal leakages and leakages through pressure reducing valve already being accounted for. Parameters shown in the model in Figure 15 remain the same as those identified and reported in Sections 4.1–4.6.

Model predicted behavior for the superposed forces are compared with experiments in Figure 16. As is amply evident, model predictions can faithfully capture all observed behavior for different rear pressures and input voltages to the servo valve. Additionally, it is evident that the superposed force output is greater than the force output by controlling either the flow through the servo valve (see Figure 11) or flow to the rear chamber (see Figure 14). Seeing how the superposed response of both the models accounts for nonlinearities in the resulting static force behavior of the actuator, it is reasonable to conclude that both the expanded nonlinear static force models of the actuator are validated. Furthermore, such systematic characterization of superposed behavior is also a new contribution to the literature.

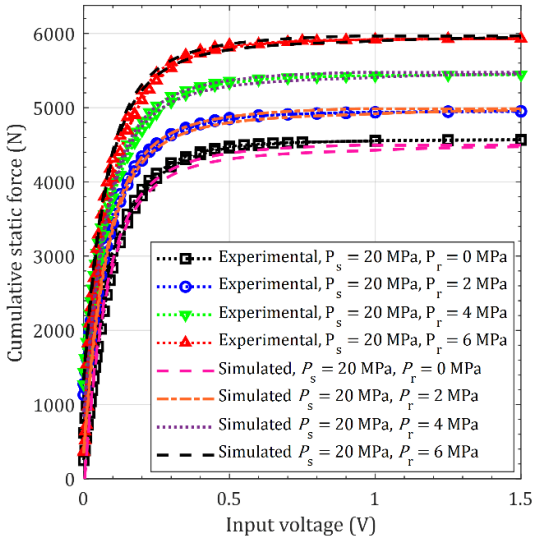

Figure 16. Experimental and simulated cumulative static force response operating with servo valve in conjunction with rear pressure.

Having characterized the static behavior and having presented expanded models to describe the observed nonlinearities, we now move our attention to characterizing the dynamic behavior of the valve-controlled actuator.

5. Dynamic Force Characterization of the Actuator and Model Parameter Identification

This section first discusses the dynamical experimental characterization of the actuator followed by discussions on system identification such that the updated dynamic force model can then be used effectively to design closed-loop control strategies discussed in Section 6.

5.1. Dynamical Experimental Characterization of the Actuator

Experiments were conducted by superimposing different levels of dynamic forces over the static forces. The static forces were first applied by controlling flow through the servo valve only. Separate experiments were also conducted by superimposing dynamic forces over the superposition of static forces applied by controlling flow to the servo valve and by also supplying pressurized flow to the rear chamber.

For the first case, i.e., for force controlled through the servo valve, a dynamic 100 mV AC signal was superimposed upon a static 200 mV DC signal. For the second case, the servo valve was supplied a dynamic 100 mV AC signal that was superimposed upon a static 200 mV DC signal, that in turn was superposed over the force due to pressurized flow supplied to the rear chamber, wherein the pressure in the rear chamber was controlled to be 10 MPa. The AC/DC voltages supplied to the system were selected such as to not saturate the actuator. For all cases, the system was excited for 30 s using a sine chirp signal ranging from 1 Hz to 300 Hz. The output from the load cell and the input voltage were logged, and as examples, the data acquired for the first two seconds has been shown in Figure 17. The input voltage is shown in Figure 17a, and the measured forces are shown in Figure 17b,d. Since the force applied by the actuator is a superposition of the static and dynamic components, and since the static behavior has already been characterized systematically in Section 4, and since this section is only concerned with characterizing the dynamic behavior, the static force was subtracted from the measured output force signal, and that is also shown in Figure 17c,e. As is evident from Figure 17b which shows the dynamic force superimposed over the servo valve controlled static force, and from Figure 17d which shows the dynamic force superimposed over the superposition of the servo valve controlled static force along with the force due to pressurized fluid in the rear chamber, in the latter case, the net force applied by the actuator is greater, and this is consistent with the static

analysis presented in Section 4. Additionally, it is evident that on subtraction of the static forces, the dynamic component of the forces for both cases are similar—see Figure 17c,e.

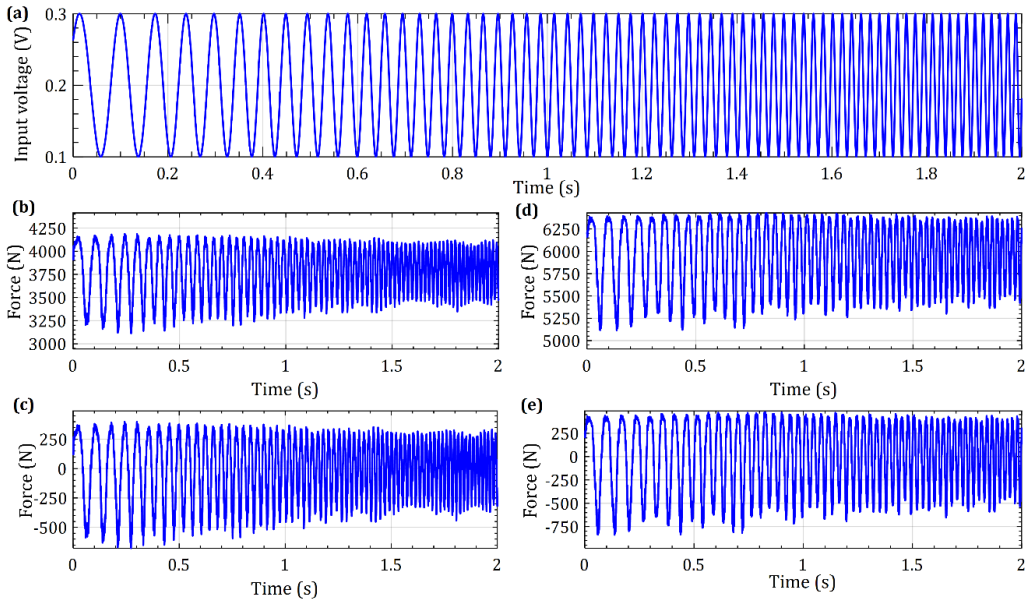

Figure 17. Supplied voltage and measured force signals for different experimental conditions; (**a**) input voltage to the servo valve-100 mV AC and 200 mV DC; (**b**) measured static and dynamic force controlled by servo valve; (**c**) measured dynamic force with subtracted static force controlled by servo valve; (**d**) measured static and dynamic force controlled by servo valve + pressure in the rear chamber; (**e**) measured dynamic force with subtracted static force controlled by servo valve + pressure in the rear chamber.

The dynamic component of the signals was post-processed in MATLAB to obtain the open-loop frequency response of the actuator that is shown in Figure 18a. The frequency response function shown in Figure 18a is only for the case of the flow controlled through the servo valve. Results for flow through the servo valve and to the rear chamber are shown in Figure 18b, which also shows the dynamic characteristics for different levels of input voltages supplied to the servo valve. Since the raw data was observed to be noisy—see Figure 18a, it was filtered using a Savitsky–Golay first-order moving average filter, and the filtered frequency response of the actuator is overlaid in Figure 18a, and all responses shown in Figure 18b are filtered.

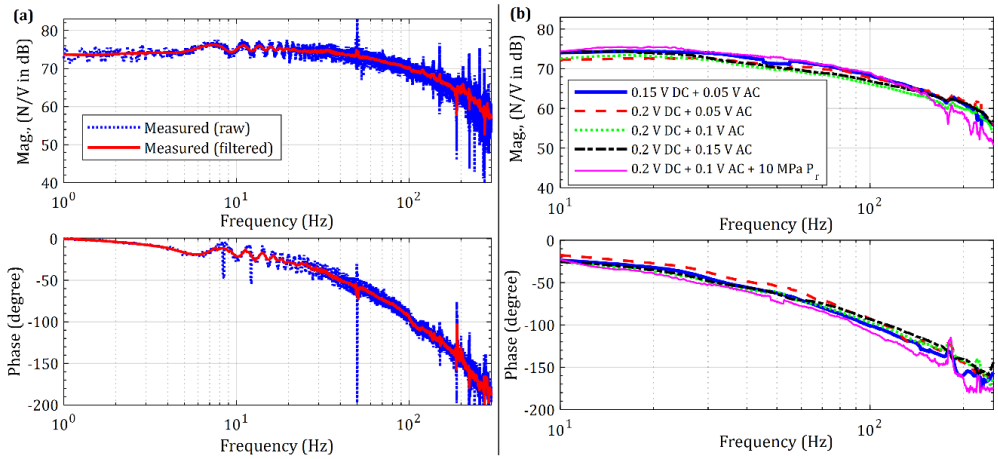

Figure 18. Measured open-loop frequency response of the actuator under different test conditions; (**a**) measured and filtered measured frequency response; (**b**) filtered measured frequency responses at different levels of input voltages showing linear dynamic response of the actuator.

As is amply evident from Figure 18, the open-loop frequency response of the actuator at different levels of input voltages to the servo valve with/without the rear pressure exhibit similar response characteristics. This suggests that the dynamic force response of the actuator is indeed linear, and the nonlinearities are mostly due to its static behavior that have been already described in Section 4. The open-loop frequency response of the actuator shown in Figure 18 suggests that the actuator has a very high open-loop gain, and that its bandwidth is less than 50 Hz—which is inadequate for structural testing of machine tools that the actuator is meant for. To implement closed-loop control of the actuator to increase its bandwidth, we adopt a model-based tuning approach that will guide closed-loop experiments, for which we first update the model described in Section 3.1 to match the measured behavior—as is discussed next.

5.2. System Identification and Updating the Dynamical Force Model

To characterize the dynamic behavior of the actuator, there remain elements in the model described in Section 3.1 and in Equation (17) that must be experimentally identified. The parameters to be identified include the linearized constant value of flow-pressure coefficient, the load stiffness, the viscous damping coefficient, and the valve's natural frequency and damping ratio. To identify these parameters, we formulate an optimization problem to estimate the unknown model parameters of the actuator. The cost function is obtained as the error between the estimated transfer function from the measured data $G_{\text{force,measured}}$, and the model-based transfer function $G_{\text{force,modelled}}$ [13]:

$$f_{\text{obj}} = \frac{1}{n}\sum_{i=1}^{n} |G_{\text{force,measured}}(s) - G_{\text{force,modelled}}(s)|^2 \text{ such that } x_{lb} \le x \le x_{ub} \tag{44}$$

where in, $s = \text{j}\omega, \{\omega \to 2\pi(1 \le 0.5 \le 300)\ \text{rad/s}\}$ (j is the imaginary unit), $x \in \{K_{\text{Ct}}, K_{\text{L}}, C, \omega_{\text{nv}}, \zeta\}$, and n is the number of discrete points contained in ω. Subscripts *lb* and *ub* corresponds to the lower bound and upper bound of the unknown variables (x) respectively. To minimize f_{obj}, we solve the constrained minimization problem using MATLAB's *fmincon* function running the interior-point algorithm. Since the performance of such gradient-based algorithms are sensitive to starting points, it is difficult to guarantee that even a local minimum has been reached. Hence, we instead use convergence of the cost function as a stopping criterion to find the unknown model parameters $\{K_{\text{Ct}}, K_{\text{L}}, C, \omega_{\text{nv}}, \zeta\}$, and select the starting values to be physically meaningful, and further limit the lower bounds (*lb*) and the upper bounds (*ub*) to be within $\pm\,50\%$ of the initial guess.

Since convergence of the optimization problem is sensitive to the initial guess of the parameters, an estimate of the order of valve's natural frequency (ω_{nv}), damping ratio (ζ), and valve flow-pressure coefficient (K_{Ct}) was taken from the datasheet of servo valve [48,49]. Although the flow-pressure coefficient was identified to be nonlinear in Section 4.2.1, but since its nonlinearity has already been accounted for in the static analysis therein, it is assumed to be constant here, under the linearized assumptions stated earlier in Section 3.1. The stiffness constant, K_{L} was estimated from a static stiffness simulation while other design parameters, such as the area of the piston annulus, the volume of the chamber, and the moving mass which includes the load cell and the translating mass of the piston along with the fluid around the piston rod, were already known beforehand. The effective bulk modulus of the servo oil (servo grade 32) at the supply pressure of 20 MPa was calculated based on the analysis presented in [50].

The identified unknown model parameters are listed in Table 1. The flow gain coefficient K_{Qv} listed in Table 1 is the product of the servo gain (K_{v}) and of the flow coefficient (K_{Q}). As is evident from the comparison of the converged values in Table 1, only the flow-pressure coefficient settles at a value that is an order of magnitude different than the initial guess, suggesting that the dynamical response of the system is most sensitive to this coefficient.

A check of the Hessian of the cost function at the converged values shows one of the eigenvalues of the Hessian to be zero, two to be negative, and four to be positive—suggesting further that the Hessian is indefinite and that the converged values do not correspond to a local minimum. The use of more robust optimization algorithms may have guaranteed at least a local minimum. However, even though a local minimum was not found, the model predicted response using the identified

parameters agrees with the measured response–as shown in Figure 19, and hence the identified parameters and method of minimization were deemed acceptable.

Seeing how the dynamical model is validated, this model is now used to tune the closed-loop control to target an increase in the bandwidth of the actuator from being less than 50 Hz to increase to ~200 Hz–such that the actuator may then prove effective for structural testing of machine tools.

Table 1. Model parameters of the electro-hydraulic actuator system.

Variables	Symbol	Value	
		Initial value	Converged value
Effective translating mass	M [kg]	0.893	–
Area of piston	A_p [m^2]	2.364×10^{-4}	–
Piston chamber volume	V_t [m^3]	2.364×10^{-6}	–
Effective bulk modulus of oil	β_e [N/m^2]	1.75×10^{9}	–
Flow gain coefficient	K_{Qv} [$m^2/s/V$]	3.33×10^{-3}	–
Actuator static stiffness	K_L [N/m]	4.83×10^{8}	4.83×10^{8}
Viscous damping coefficient	C [Ns/m]	10	10.587
Total flow-pressure coefficient	K_{Ct} [$m^3/s/Pa$]	1.6585×10^{-11}	1.51×10^{-10}
Valve natural frequency	ω_{nv} [rad/s]	1500	1507.9
Valve damping ratio	ζ	0.7	0.59

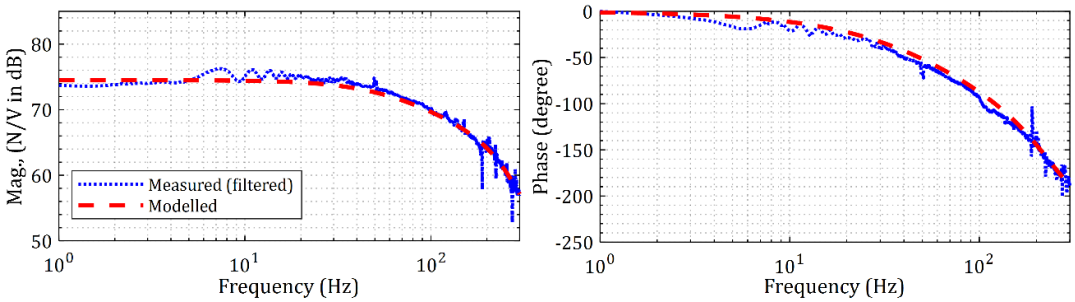

Figure 19. Comparison of open-loop experimental and modelled transfer function between input to the valve and actuator output force.

6. Closed-loop Control of the Actuator

This section first discusses the use of the expanded and validated static and dynamic models to tune controller gains before discussing its practical implementation. Closed-loop control of only the servo valve based static and dynamic force response is considered herein, since the pressured flow supplied to the rear chamber is not automatically controllable. Owing to the ease of tuning and implementation, investigations herein are limited to using only a PI control strategy based on force feedback, and other advanced control designs are left for future investigations.

6.1. Model-Based Closed-Loop Control Investigations

Since the force models for static (see Section 4.3) and dynamic (see Section 3) applications are different, the PI controller gains are tuned separately for both models. Model-based tuning is carried out using MATLAB's auto-tuner toolbox. The Simulink model for closed-loop control of the actuator is shown in Figure 20a for the static case, and in Figure 20b for the dynamic case, in which $g_{VN} = 0.5097$ mV/N is the sensitivity of the load cell. Since the measured force characteristics in the open-loop characterization discussed in Section 4 and 5 were observed to be corrupted by noise, and were also observed to have some inexplicable frequency content at 225 Hz and at 420 Hz, for the model-based controller tuning to be representative of experimental conditions, these signals were also

modelled as shown in Figure 20a,b. Since no filters were used to condition the real measured signals, the model tool does not include any filters.

The tuned PI gains for nonlinear static force model are found to be p = 5.61e−6 and I = 10000, and for linearized dynamic force model were found to be p = 0.57 and I = 386.24. With these PI gains, all poles for the closed-loop control of the static and the dynamic models were found to lie in the left-half of the s-plane–suggesting stability of both the closed-loop systems.

For control of the static model with the tuned PI gains, the gain margin was evaluated to be infinite, and the phase margin was found to be 90°. These large gain and phase margins suggest that even though the system is stable, its response is sluggish—which is indeed confirmed by the step responses shown in Figure 20c. Since the static model has nonlinearities, the simple PI based linear controller is clearly inadequate, and, and future investigations may consider the use of other advanced controller implementations.

For the case of the control of the dynamic model with tuned PI gains, the gain margin was evaluated to be 10.8 dB, and the phase margin was found to be 60°, and the corresponding gain cross-over frequency and the phase cross-over frequency was found to be 262.6 Hz and 99.63 Hz, respectively. These gain and phase margins are lesser than the those for the static case, and hence, the step response for the dynamic case is less sluggish, but is still oscillatory in nature, as is evident from the step response shown in Figure 20c. The gain and phase margins and the oscillatory response clearly suggest that there is yet scope to improve the controlled performance using advanced control strategies, and that too may well form part of future investigations. However, since the tuned PI controller based on the linearized dynamic force model takes only 7 ms to achieve the steady state, it is deemed adequate, and these model-based gains are used to instruct the closed-loop experimentation as is discussed next.

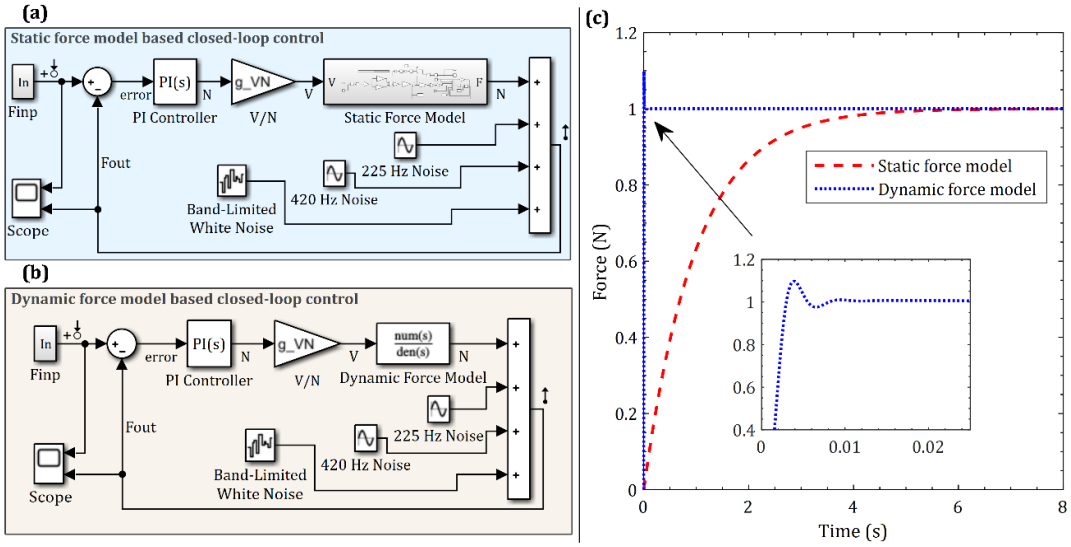

Figure 20. Model-based closed-loop control of the actuator; (**a**) Simulink model for static force model based closed-loop control; (**b**) Simulink model for dynamic force model based closed-loop control; (**c**) closed-loop step response of actuator using static and dynamic force models.

6.2. Closed-loop Control Experiments

For closed-loop experiments, the PI controller is implemented in the FPGA LabVIEW program (see Figure 3). The control loop runs at a 5 kHz sampling rate and a controlled voltage signal is sent to the servo valve through the analogue output module installed in the cRIO controller. Since the FPGA LabVIEW program implements a discrete PI controller, the model-based PI gains are normalized, where in the proportional gain remains $K_P = P \equiv 0.57$, and the integral gain in the discretized mode becomes $K_i = K_P T_s/T_i$, where T_s is sampling time of the controller, and $T_i = 1/I$, where I is the model-based integral gain, which was tuned to be 386.24. Though these model-based

gains were used as initial parameters to control the actuator, experiments with a proportional gain (K_P) of 0.4 and an integral gain (T_i) of 10^{-4} were found to exhibit better force control. Experiments with these calibrated gains were then conducted to apply a target static load of 785 N that was to be superposed with a ± 196 N dynamic force in the frequency range of 1 Hz to 300 Hz. This reference force is shown in Figure 21a. The model-based force tracking of this reference is shown in Figure 21b, and the measured force tracking of the reference input is shown in Figure 21c. The closed-loop simulation and experiment runs for 300 s, with each second of data corresponding to each excitation frequency in the range of 1 Hz to 300 Hz.

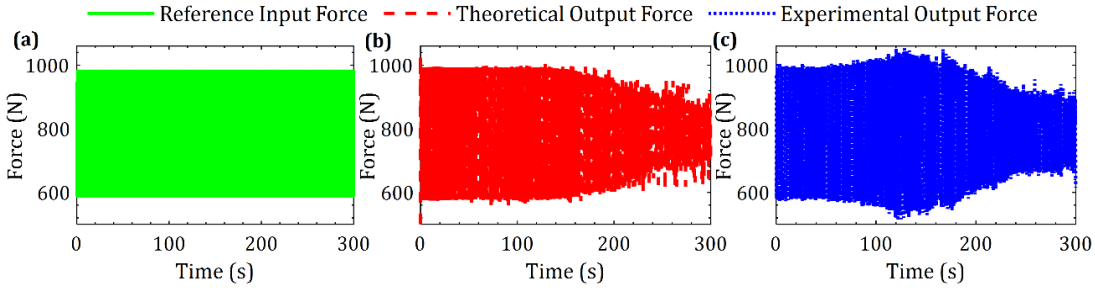

Figure 21. Theoretical and experimental closed-loop force response: (**a**) reference input force; (**b**) theoretical output force; (**c**) experimental output force.

As is evident from Figure 21, the modelled and measured force response closely track the reference input force till ~200 Hz (~200 s), beyond which the magnitude of force response is significantly reduced. The operating closed-loop bandwidth of the actuator is identified by transforming the time domain data presented in Figure 21 into the frequency response function as shown in Figure 22.

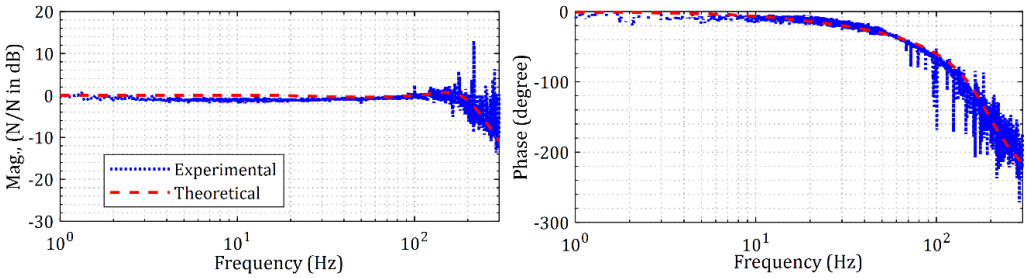

Figure 22. The experimental and theoretical closed-loop frequency response of the electro-hydraulic actuator.

As is amply evident from Figure 22, the bandwidth of the electro-hydraulic actuator is significantly improved to 200 Hz in closed-loop as compared to the open-loop bandwidth being less than 50 Hz. Also evident is that the theoretically predicted frequency response based on the updated dynamic force model captures the measured frequency response of the electro-hydraulic actuator. However, a phase lag between the input and the output force response is observed in both the simulation and experimental results. This phase lag can be compensated using a well-designed phase lead compensator, which can be part of future studies.

In addition to characterizing the bandwidth of the actuator, force responses for different kinds of step loading and for different kinds of fixed frequency excitations were investigated to further validate the closed-loop performance of the actuator. These results, as shown in Figure 23, include step loading scenarios with increasing step loads (Figure 23a), decreasing step loads (Figure 23b), random step loads (Figure 23c), and fixed frequency excitations for 785 N static loads superposed with ± 196 N sinusoidal dynamic loads at three different frequencies—at 10 Hz (Figure 23d) and at 120 Hz (Figure 23e), which as well is within the bandwidth, and at 210 Hz (Figure 23f), which is marginally beyond the actuator

bandwidth. Experimental results in Figure 23 also depict the reference target loads as well as the model-predicted tracking loads to make comparisons more meaningful.

As is evident from Figure 23, the experimental results for the step loading scenarios compare very well with the reference input as well as with the model-predicted response. This suggests that using a single set of controller gains tuned for the dynamic response, also work well for the quasi-static step loading cases. Furthermore, the static loads superposed with dynamic loads at different frequencies confirm the phase behavior observed in Figure 22, i.e., as the frequencies of excitation increase, there is a noticeable phase lag in the system (see Figure 23e,f), and at excitation frequencies beyond the bandwidth (Figure 23f), there is also a noticeable reduction in the amplitude of measured force characteristics in comparison to the reference target loads. Moreover, for both types of loading scenarios, it is further evident that the model-based force control can reasonably track the commanded reference, and the measured closed-loop behavior.

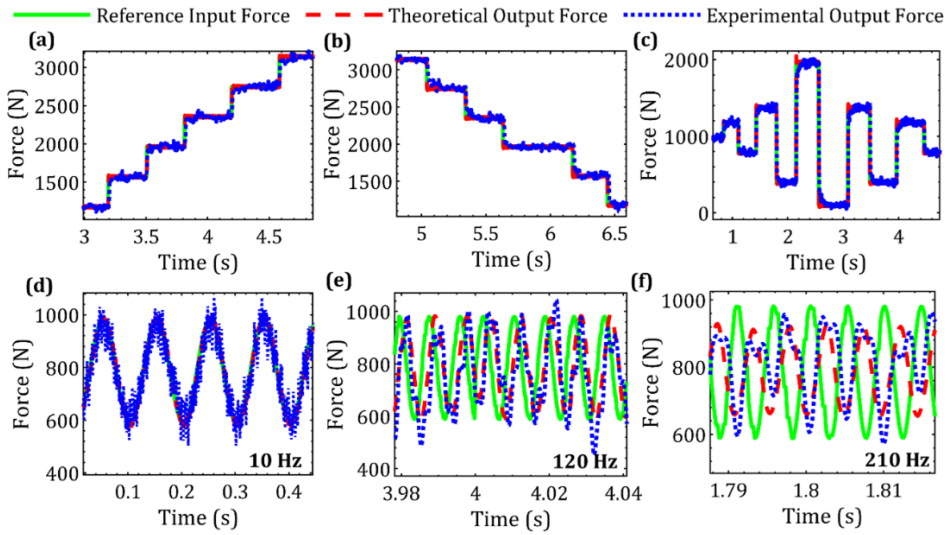

Figure 23. Theoretically predicted and experimental force response: (**a**–**c**) increasing, decreasing, and random step load, respectively; (**d**–**f**) sine load with 785 N static and ± 196 N dynamic force at 10 Hz, 120 Hz and 210 Hz, respectively.

Since the nonlinear static and linearized dynamic models have both been validated, and seeing that the model-based controlled behavior also matches experimental observations, the models presented in this paper can be used to further guide design improvements of electro-hydraulic actuators, as desired. Additionally, although a simple PI controller was found effective to increase the bandwidth of the actuator to 200 Hz, issues with phase lag still need to be addressed, and that too can form part of future research investigations.

7. Conclusions

This paper discussed the characterization of the static, dynamic, and closed-loop control behavior of a newly developed compact electro-hydraulic actuator that consists of a double-acting piston and cylinder arrangement controlled by a servo valve, and a separate rear chamber controlled by a separate valve that are designed to work in conjunction to generate static forces up to 7000 N that can be superposed with dynamic forces of up to ± 1500 N. The actuator was characterized to evaluate its suitability for machine tool structural testing, and the actuator's ability to superpose periodic forces over a non-zero mean makes it capable of applying realistic loading conditions like those experienced by machines during cutting processes.

Experiments to characterize the static behavior of the actuator show it to exhibit nonlinearities for when the actuator is controlled by the servo valve, and separately for when pressurized flow is

supplied to the rear chamber. Static experiments that superpose forces obtained from controlling the servo valve with those obtained from controlling pressure in the rear chamber also exhibit nonlinearities. Since linearized static models were found to be inadequate to capture the observed nonlinear behavior, the static force models were expanded to include nonlinearities due to dead-bands, nonlinearities due to hysteresis of the electrical and mechanical kinds, nonlinearities in the flow-pressure characteristics, nonlinearities due to static, Coulombic and viscous friction, nonlinearities causing saturation of forces, and nonlinearities due to no-load flow and leakages in the system. Predictions with the expanded nonlinear static force models were found to agree with experimental observations for the valve controlled actuator and for the case of pressurized fluid supplied to the rear chamber, as well as for the case of forces being a superposition of those obtained from controlling the servo valve with those obtained from controlling pressure in the rear chamber. Such expanded model-based characterization of all the major nonlinearities in the system for such electro-hydraulic actuators is thought to be a new contribution to the literature.

Experiments to characterize the dynamical behavior of the actuator under different loading scenarios, i.e., by superimposing dynamic forces over static forces, including superposition of dynamic forces over valve-controlled static forces and over the superposition of static forces applied through flow to the servo valve and with pressurized flow to the rear chamber—showed the actuator to behave linearly, which suggested that the proposed linear model adequately describes the actuator's dynamic response. Such systematic model-based characterization supported by experiments of the static and dynamic behavior of electro-hydraulic actuators to evaluate their suitability for machine tool structural testing is also a new contribution to the literature.

Since the open-loop dynamic behavior of the actuator was observed to have a high gain, and a bandwidth of less than 50 Hz, the validated static and dynamic force models were used to develop a model-based tuning strategy, which in turn guided the closed-loop experiments. Closed-loop control based on tuning a simple proportional-integral (PI) controller increased the bandwidth up to 200 Hz–making the actuator more suitable for its intended application of machine tool structural testing. Though closed-loop control increased the bandwidth significantly, yet issues related to the observed phase lags at higher frequencies still need to be addressed.

The validated models presented herein can instruct the design and development of other higher-performance electro-hydraulic actuators—even for other applications, and, can also guide the conversion of the actuator into a damper, and to also test other advanced control strategies to further improve actuator performance.

Author Contributions: Conceptualization, G.N.S, S.S., A.S., and M.L.; methodology, G.N.S., S.S., and A.S.; software, G.N.S., S.S., and A.S.; validation, G.N.S., S.S., and A.S.; formal analysis, G.N.S., S.S., and A.S.; investigation, G.N.S, S.S., and A.S.; resources, M.L.; data curation, G.N.S., S.S., and A.S.; writing—original draft preparation, G.N.S., S.S., and A.S.; writing—review and editing, G.N.S., S.S., A.S. and M.L.; visualization, G.N.S., S.S., and A.S.; supervision, M.L. All authors have read and agreed to the published version of the manuscript.

Funding: This research was funded by Government of India's Impacting Research Innovation and Technology (IMPRINT), through project number IMPRINT 5509.

Conflicts of Interest: The authors declare no conflict of interest.

References

1. Merritt, H.E. *Hydraulic Control. Systems*; John Wiley & Sons: Hoboken, NJ, USA; 1967.
2. Jelali, M.; Kroll, A. *Hydraulic Servo-Systems: Modelling, Identification and Control*; Springer Science & Business Media: Berlin, Germany, 2003.
3. Salleh, S.; Rahmat, M.F.; Othman, S.M.; Danapalasingam, K.A. Review on modeling and controller design of hydraulic actuator systems. *Int. J. Smart Sens. Intell. Syst.* **2015**, *8*, 338–367.
4. Edge, KA. The control of fluid power systems-responding to the challenges. *Proc. Inst. Mech. Eng. Part. I J. Syst. Control. Eng.* **1997,** ,*211*, 91–110, doi:10.1243%2F0959651971539920.
5. Spencer, R. Applying the Electro-Hydraulic Servo Valve to Industry. *IRE Trans. Ind. Electron.* **1958**, *PGIE-7*, 33–39.

6. Srinivasan, K.; Dogan, C. Digital Control Algorithms for Electrohydraulic Machine Tool Feed Drive Servomechanisms In Proceedings of the 1984 American Control Conference, San Diego, CA, USA, 6–8 June 1984; pp. 449–457.
7. Altintas, Y.; Verl, A.; Brecher, C.; Uriarte, L.; Pritschow, G. Machine tool feed drives. *CIRP Ann*. **2011**, *60*, 779–796.
8. Altintas, Y.; Ber, A.A. Manufacturing Automation: Metal Cutting Mechanics, Machine tool Vibrations, and CNC Design. *Appl. Mech. Rev.* **2001**, *54*, B84–B84.
9. Brecher, C.; Schulz, A.; Week, M. Electrohydraulic active damping system. *CIRP Ann.* **2005**, *54*,389–392, doi:10.1016/S0007-8506(07)60129-2.
10. Brecher, C.; Manoharan, D.; Klein, W. Active compensation for portal machines. *Product. Eng.* **2010**, *4*, 255–60, doi:10.1007/s11740-010-0212-y.
11. Brecher, C.; Fey, M.; Brockmann, B.; Chavan, P. Multivariable control of active vibration compensation modules of a portal milling machine. *J. Vib. Control*. **2018**, *24*, 3–17, doi:10.1177/1077546316636519.
12. Wabner, M.; Law, M.; Ihlenfeldt, S. Dynamic modelling of an electro-hydraulic actuator to isolate machine tools from ground vibrations. In Proceedings of the 11th International Conference on High Speed Machining (HSM 2014): Advances in Manufacturing Technology, Prague, Czech Republic, 11–12 September 2014.
13. Law, M.; Wabner, M.; Colditz, A.; Kolouch, M.; Noack, S.; Ihlenfeldt, S. Active vibration isolation of machine tools using an electro-hydraulic actuator. *CIRP J. Manuf. Sci. Technol.* **2015**, *10*, 36–48, doi:10.1016/j.cirpj.2015.05.005.
14. Law, M. Design Guidelines for an Electro-Hydraulic Actuator to Isolate Machines from Vibrations. 6th International & 27th All India Manufacturing Technology, Design and Research Conference (AIMTDR2016), Pune, India, 16–18 December 2016.
15. Thampy, T.; Kumar, M.; Ragavendra, D.R.; Maanasan, M.; Kumar, K. *Design and Development of Electro Hydraulic Force Exciter*; 2014; pp. 1–6.
16. Plummer, A.R. Control techniques for structural testing: A review. *Proc. Inst. Mech. Eng. Part. I J. Syst. Control. Eng.* **2007**, *221*,139–169, doi:10.1243/09596518JSCE295.
17. Zhang, L.; Cong, D.; Yang, Z.; Zhang, Y.; Han, J. Optimal design and hybrid control for the electro-hydraulic dual-shaking table system. *Appl. Sci*. **2016**, *6*, 220, doi:10.3390/app6080220.
18. Chaudhuri, A.; Wereley, N. Compact hybrid electrohydraulic actuators using smart materials: A review. *J. Intell. Mater. Syst. Struct.* **2012**, *23*, 597–634, doi:10.1177/1045389X11418862.
19. Alle, N.; Hiremath, S.S.; Makaram, S.; Subramaniam, K.; Talukdar, A. Review on electro hydrostatic actuator for flight control. *Int. J. Fluid Power* **2016**, *17*,125–45, doi:10.1080/14399776.2016.1169743.
20. Yang, H.Y.; Pan, M. Engineering research in fluid power: A review. *J. Zhejiang Univ. Sci. A* **2015**, *16*,427–42, doi:10.1631/jzus.A1500042.
21. Moog Inc. Electrohydraulic Valves: A Technical Look. Available online: https://www.moog.com/literature/ICD/Valves-Introduction.pdf. (accessed on 23 June 2020).
22. Tamburrano, P.; Plummer, A.R.; Distaso, E.; Amirante, R. A review of electro-hydraulic servovalve research and development. *Int. J. Fluid Power* **2018**, *20*, 1–23.
23. Boulet, B.; Daneshmend, L.; Hayward, V.; Nemri, C. *System Identification and Modelling of a High Performance Hydraulic Actuator*; Springer: Berlin/Heidelberg Germany, 1993; pp. 503–520.
24. Habibi, S.; Goldenberg, A. A mechatronics approach for the design of a new high performance electrohydraulic actuator. *SAE Trans*. **1999** ,353–360, doi:10.4271/1999-01-2853.
25. Efe, Y. Dynamic Model of a Hydraulic Servo System for a Manipulator Robot, Master's Thesis, School of Industrial Engineering and Management, Stockholm, Sweden 2014. Available online: http://urn.kb.se/resolve?urn=urn%3Anbn%3Ase%3Akth%3Adiva-152800. (accessed on 24 June 2020).
26. Rydberg, K.-E. Hydraulic Servo Systems: Dynamic Properties and Control, Linköping University 2016. Available online: http://urn.kb.se/resolve?urn=urn:nbn:se:liu:diva-132396. (accessed on 23 June 2020).
27. Eryilmaz, B.; Wilson, B.H. Modeling the internal leakage of hydraulic servovalves. *Int. Mech. Eng. Cong. Expo. ASME* **2000**, *69*, 337–343.
28. Jianyong, YA.; Zongxia JI.; Bin, YA. Robust control for static loading of electro-hydraulic load simulator with friction compensation. *Chin. J. Aeronaut*. **2012**, *25*, 954–962, doi:10.1016/S1000-9361(11)60467-6.
29. Das, J.; Mishra, S.K.; Saha, R.; Mookherjee, S.; Sanyal, D. Actuation dynamic modeling and characterization of an electrohydraulic system. *Proc. Inst. Mech. Eng. Part. I J. Syst. Control. Eng.* **2016**, *230*, 537–550, doi:10.1177/0959651816636315.

30. Wang, G.; Wei, J.; Fang, J.; Shi, W.; Zhang, Q. Modelling and experimental verification of pressure relief synchronous control for small trapped fluid volumes. *Trans. Inst. Meas. Control* **2018**, *40*, 2960–2969.
31. Yuan, H.; Na, H.; Kim, Y. System identification and robust position control for electro-hydraulic servo system using hybrid model predictive control, *J. Vib. Control* **2018**, *24*, 4145–4159, doi:10.1177/1077546317721417.
32. Brian, E.S. Research for Dynamic Seal Friction Modeling in Linear Motion Hydraulic Piston Applications. Master's Thesis, The University of Texas at Arlington, Arlington, TX, USA, 2005. Available online: http://hdl.handle.net/10106/471. (accessed on 24 June 2020).
33. Liu, Y.F.; Li, J.; Zhang, Z.M.; Hu, X.H.; Zhang, W.J. Experimental comparison of five friction models on the same test-bed of the micro stick-slip motion system. *Mech. Sci*. **2015**, *6*, 15, doi:10.5194/ms-6-15-2015.
34. Armstrong-He´ louvry, B.; Dupont, P.; Canudas de Wit, C. Friction in servo machines: Analysis and control methods. *Appl. Mech. Rev.* **1994**, *47*, 275–305, doi:10.1115/1.3111082.
35. Liu, R.; Alleyne, A. Nonlinear force/pressure tracking of an electro-hydraulic actuator. *J. Dyn. Sys., Meas. Control.* **2000**, *122*, 232–236, doi:10.1115/1.482466.
36. Andersson, S.; Söderberg, A.; Björklund, S. Friction models for sliding dry, boundary and mixed lubricated contacts. *Tribol. Int.* **2007**, *40*, 580–587, doi:10.1016/j.triboint.2005.11.014.
37. Chen, Z.; Wang, W. Analysis of Temperature Characteristics of Electro-hydraulic Servo Valve Based on AMESim, In Proceedings of the International Conference on Mechanical, Electrical, Electronic Engineering and Science (MEEES 2018), Chongqing, China 26–27 May 2018; Atlantis Press: Paris, France, 2018; dx.doi:10.2991/meees-18.2018.10.
38. Kim, A. Linearized Electrohydraulic Servovalve Model for Valve Dynamics Sensitivity Analysis and Control System Design. *J. Dyn. Syst. Meas. Control Trans. ASME* **2000**, *122*, 179–187.
39. Xuan, J.; Wang, S. Development of hydraulically driven fatigue testing machine for insulators. *IEEE Access*. **2017**, *6*, 980–988, doi:10.1109/ACCESS.2017.2777103.
40. Xuan, J.; Wang, S.; Liu, H. Design and control of a hydraulic composite actuator for vibration simulation. *Adv. Mech. Eng*. **2018**, *10*, 168781401877380, doi:10.1177/1687814018773809.
41. Zhu, Y.; Tang, S.; Wang, C.; Jiang, W.; Zhao, J.; Li, G. Absolute stability condition derivation for position closed-loop system in hydraulic automatic gauge control. *Processes* **2019**, *7*, 766.
42. Zulaika, J.J.; Campa, F.J.; De Lacalle, L.L. An integrated process–machine approach for designing productive and lightweight milling machines. *Int. J. Mach. Tools Manuf.* **2011**, *51*, 591–604.
43. Niksefat, N.; Sepehri, N. Design and experimental evaluation of a robust force controller for an electro-hydraulic actuator via quantitative feedback theory. *Control. Eng. Pract.* **2000**, *8*,1335–1345, doi:10.1016/S0967-0661(00)00075-7.
44. Nakkarat, P.; Kuntanapreeda, S. Observer-based backstepping force control of an electrohydraulic actuator. *Control Eng. Pract.* **2009**, *17*, 895–902, doi:10.1016/j.conengprac.2009.02.011.
45. Jianyong, Y.; Zongxia, J.; Bin, Y.; Yaoxing, S.; Wenbin, D. Nonlinear adaptive robust force control of hydraulic load simulator. *Chin. J Aeronauti.* **2012**, *25*, 766–775, doi:10.1016/S1000-9361(11)60443-3.
46. Kang, S.; Yan, H.; Dong, L.; Li, C. Finite-time adaptive sliding mode force control for electro-hydraulic load simulator based on improved GMS friction model. *Mech. Syst. Sig. Proc.* **2018**, *102*, 117–138, doi:10.1016/j.ymssp.2017.09.009.
47. Li, X.; Zhu, Z.C.; Rui, G.C.; Cheng, D.; Shen, G.; Tang, Y. Force loading tracking control of an electro-hydraulic actuator based on a nonlinear adaptive fuzzy backstepping control scheme. *Symmetry* **2018**, *10*, 155.
48. Bosch Rexroth AG, Datasheet: Servo directional valve of 4-way design, Lohr am Main, Germany: Bosch Rexroth Proportional, High-Response and Servo Valves Catalogue, 2018. Available online: https://www.theseus.fi/bitstream/handle/10024/58216/4%20WS%202%20EM.PDF?sequence=1&isAllowed=y (accessed on 22 June 2020).

49. Moog Controls Inc. Transfer functions for Moog Servovalves, Technical Bulletin, 1965. Available online: https://csl-ep.mech.ntua.gr/Intranet/Info_Manuals/Hydraulics/Moog/Moog%20Technical%20Bulletins/103-Transfer%20Functions%20%20for%20Moog%20Servovalves.pdf. (accessed on 24 June 2020).
50. Sakama, S.; Tanaka, Y.; Goto, H. Mathematical model for bulk modulus of hydraulic oil containing air bubbles. *Mech. Eng. J.* **2015**, *2*, 15-00347, doi:10.1299/mej.15-00347.